SEDIMENTOLOGY the journal of the International Association of Sedimentologists IAS

Sedimentology (2026) doi: 10.1111/sed.70068

Evaluating the possible role of bottom currents and internal waves in shaping seafloor morphology in a mesophotic reef

OR M. BIALIK*,†,‡,[1], HENRIETTE WILCKENS*,[1], OMRI GADOL§,¶, AARON MICALLEF**, CHRISTIAN BETZLER††, OLE JOHANNES R. SØRENSEN‡‡, HAGAI NATIV‡‡ and YIZHAQ MAKOVSKY*,¶

**Dr. Moses Strauss Department of Marine Geosciences, The Leon H. Charney School of Marine Sciences, University of Haifa, 199 Abba Khoushy Ave, Mount Carmel, Haifa 31905, Israel (E-mail: obialik@ocean.org.il) (E-mail: hwilcken@campus.haifa.ac.il) (E-mail: yizhaq@univ.haifa.ac.il)*

†Institute of Geology and Palaeontology, University of Münster, Corrensstr. 24, Münster 48149, Germany

‡Israel Oceanographic and Limnological Research, National Institute of Oceanography, Haifa 310800, Israel

§CERENA, Instituto Superior Técnico, Lisbon University, Av. Rovisco Pais, 1049-001, Lisbon, Portugal

¶Hatter Department of Marine Technologies, Charney School of Marine Sciences, University of Haifa, 199 Abba Khoushy Ave, Mount Carmel, Haifa 31905, Israel

***Monterey Bay Aquarium Research Institute, Moss Landing, CA, USA*

††Institute of Geology, CEN, University of Hamburg, Bundesstrasse 55, Hamburg 20146, Germany

‡‡Morris Kahn Marine Research Station, The Leon H. Charney School of Marine Sciences, University of Haifa, 199 Abba Khoushy Ave, Mount Carmel, Haifa 31905, Israel

Associate Editor: Gregor Eberli

ABSTRACT

Mesophotic reefs are located in low light conditions which, depending on the region, are usually found in water depths greater than ~30 m. They are less affected by ocean warming than reefs found in shallower water depths and thus might become increasingly important for the sustainability of marine biodiversity. Here we explore the physical mechanisms controlling the sediment distribution around a coralligenous mesophotic reef. A detailed survey of the Bustan HaGalil Ridge offshore Israel (30 to 50 m water depth) was carried out using an autonomous underwater vehicle with an interferometric synthetic aperture sonar, a multibeam echo sounder and a sub-bottom profiler. The data were combined with surface sediment samples, underwater photography, oceanographic data (measured and modelled current velocity) and water column seismic reflection data. The mesophotic reefs are built as a series of asymmetric ridges (higher slope on the north-east-facing flanks) with coarse-grained biogenic sand to gravel within the valleys between the ridges. Accumulation of sediment appears to be increased at the south-west-facing slope of the ridges compared to the north-east-facing slope. Two types of sedimentary bedforms are identified on the sediment surface: north–south elongated linear bedforms (classified as dunes) and intersecting smaller bedforms forming chevron shapes. At the western margin of the ridge, a moat-drift contourite system is identified. The oceanographic data and modelling results show a northward flowing along-slope current at the sea surface. The contourites and ridge asymmetry indicate a northward flowing bottom current. The observed dunes and chevron bedforms are attributed to

[1]These authors contributed equally to this work.

the effects of bottom currents, internal waves and their interactions. In conclusion, the geometries of the mesophotic reefs and the distribution of the sediment around them are interpreted to be controlled by internal waves and bottom currents.

Keywords Bedforms, coralline algae, Levant, sediment transport, synthetic aperture sonar.

INTRODUCTION

Benthic communities in poor light conditions that are found in depths between ca. 30 m and 150 m are commonly referred to as 'mesophotic' (Kahng *et al.*, 2010; Baker *et al.*, 2016). Mesophotic is a general term for an area where light availability is low. However, the available light conditions in different water depths vary regionally and temporarily because of changes in weather, dust storms, productivity and oceanographic processes that affect particle suspension in the water column. The exact definition of the mesophotic zone is not universally agreed upon (Bradford & Chang, 1987; Mitchell *et al.*, 2000; Brokovich *et al.*, 2008). Reefs in the mesophotic zone are often located below or on the pycnocline in waters significantly cooler and more nutrient-enriched compared to shallow reefs (Lesser *et al.*, 2018; Kahng *et al.*, 2019; Richardson & Bendtsen, 2019). Mesophotic reefs might be important refugia from environmental stress caused by climate change and anthropogenic disturbances (Bongaerts *et al.*, 2010; Martinez *et al.*, 2021; Dimitrijević *et al.*, 2024; Tsemel *et al.*, 2025). Despite their importance, mesophotic reefs are understudied compared to shallower reefs, possibly because they are more difficult to reach (Menza *et al.*, 2007; Eyal *et al.*, 2021). Mesophotic reefs exhibit a different benthic community and composition than reefs in shallower waters (Kahng *et al.*, 2014; Rocha *et al.*, 2018) and can have a significant coralline algae constituent (Amado-Filho *et al.*, 2016). This coralline component means that the sediment and framework (coralligenous) production in mesophotic carbonate factories have a significant local grain export. Encrusting coralline algae such as *Lithophyllum spp.* not only contribute substantially to carbonate production but also stabilise the substrate and facilitate coral settlement, playing a key role in maintaining structural integrity and promoting biotic colonisation within these mesophotic systems (Ballesteros *et al.*, 2006). In the Eastern Mediterranean setting, the mesophotic rocky reefs host a larger proportion of branching bryozoan and larger porifera structures compared to shallower reefs (Bell *et al.*, 2024; Morris Kahn Marine Research Station database). These larger biotas provide structural habitat heterogeneity that is crucial in supporting higher trophic level biodiversity (Cerrano *et al.*, 2010).

Sediment distribution caused by surface waves and tides has a lesser effect in mesophotic reefs than they do in shallower reefs. Instead, the seafloor morphology in mesophotic environments is affected by bottom currents, which range from slope parallel to slope perpendicular (Williams *et al.*, 1984; Church *et al.*, 1985; Silva & MacDonald, 2017; Valle-Levinson *et al.*, 2020). Ocean bottom currents flowing along a slope commonly lead to an elongated depression with an associated drift also referred to as a moat-drift system (Miramontes *et al.*, 2021; Wilckens *et al.*, 2023). However, how these currents shape and control the sediment, particles (including larvae and particulate organic matter), and nutrient transport around the reefs and their sedimentary morphology is not clear at this time. For example, the genetics of communities along mesophotic belts exhibit variable patterns (Bongaerts *et al.*, 2013; Studivan & Voss, 2018), which may relate to ecological gradients shaped by the currents or larval dispersal patterns, which are also regulated by these mechanisms. This may partly be due to variable light conditions within the reef (Laverick *et al.*, 2020), but the interaction with bottom currents can also modulate the nutrient and temperature state to a level that may result in population shifts between periods of different current regimes (James *et al.*, 1999; James & Lukasik, 2010).

Following the initial experimental work of Cacchione (1970), it has been suggested that internal waves may play a significant role in modulating turbidity, nutrients, heat and sediment distribution in mesophotic settings (Kahru, 1983; Cacchione & Drake, 1986; Wolanski & Delesalle, 1995; Pomar *et al.*, 2012; Boegman & Stastna, 2019) as well as influence the evolution of reefs (Leichter *et al.*, 1998; Wang *et al.*, 2007; Lesser

et al., 2009; Schmidt *et al.*, 2016; Pomar *et al.*, 2017; Wyatt *et al.*, 2020). Internal waves are oscillations that propagate along internal stratification boundaries in the ocean (Garrett & Munk, 1979; Munk, 1981; Helfrich & Melville, 2006; Alford *et al.*, 2016). Thus, internal waves are common at the pycnocline, where density gradients are strongest due to variations in temperature and salinity. Internal waves span a broad frequency spectrum, ranging from the local inertial period (f) to the Brunt–Väisälä (buoyancy) frequency (N). The Brunt–Väisälä frequency indicates the rate of change in temperature with depth (Alford *et al.*, 2016). These waves are mostly generated by tides but can be induced by wind as well (Nagasawa *et al.*, 2000; Polton *et al.*, 2008). Similar to waves at the ocean surface, internal waves also break, transfer energy and change frequency as they approach the seafloor. Internal waves may also break when they encounter an elevated structure, such as a reef (Davis & Monismith, 2011). These internal wave breaks are an important dissipation and mixing mechanism (Lamb, 2014). The interaction of internal waves of different frequencies with the seafloor can resuspend and redistribute sediment similarly to wind waves nearshore (Quaresma *et al.*, 2007; Boegman & Ivey, 2009; Pomar *et al.*, 2012; Cheriton *et al.*, 2014). In addition to turbulence, breaking internal waves can redistribute heat and nutrients, significantly impacting deeper shelf/upper slope benthic communities (Woodson, 2018). However, how these waves interact with the seafloor in the mesophotic environment is poorly understood, as is the nature and type of bedforms they form (Morsilli & Pomar, 2012; van Haren, 2017). Several studies have suggested that internal waves lead to the formation of sediment waves (Kolla *et al.*, 1980; Droghei *et al.*, 2016; Ribó *et al.*, 2017; Reiche *et al.*, 2018). With increasing stratification of the ocean because of a change in temperature (Li *et al.*, 2020), internal waves might become increasingly important in shaping reefs as well.

The nature of seafloor interaction with both bottom currents and internal waves in the mesophotic setting needs to be better understood for predicting their future development, as well as their sustainability. The aim of this study was to examine the role of bottom currents and internal waves in a mesophotic reef. Multiple datasets from the Bustan HaGalil Ridge offshore northern Israel (southeastern Mediterranean) were used to document sediment distribution and bedforms within a mesophotic reef system.

OCEANOGRAPHIC AND GEOLOGICAL SETTING

Sediment distribution along the south-eastern margin of the Levant Basin is controlled by a geostrophic current flowing northwards (Fig. 1A), with a seasonally changing transport component generated in shallower (<15 m depth) water by wave action (Almagor *et al.*, 2000). The Levant Basin hosts several water masses that show seasonal depth variability (Alhammoud *et al.*, 2005; Sisma-Ventura *et al.*, 2016). During summer, the upper portion of the water column comprises two water masses. The warm and saline Levant Surface Water (LSW) is located between water depths of 0 and ca. 60 m, and the cooler and less saline Modified Atlantic Water (MAW) flows between water depths of 10 to 150 m. During winter, these two layers become mixed (Fig. 1C and D). These water masses are underlain by the Levantine Intermediate Water (LIW) at depths of ca. 150 to 350 m, which oscillates on an interannual scale (Ozer *et al.*, 2017). Internal waves propagate at the density boundary between the water masses and interact with the seafloor where they create sediment waves offshore Israel (Reiche *et al.*, 2018). The knowledge of the range, depth distribution, and wavelength in the region is an evolving topic. An internal wave field with a wavelength of 2.6 to 5.5 km has already been estimated in the 1990s (Pelinovksy *et al.*, 1995). Yet, this has been significantly refined in recent years. More modern studies at the Levant margin using mooring data from the DeepLev station show that internal waves have a wide frequency spectrum (Solodoch *et al.*, 2023). In this frequency spectrum, a long tail of shorter wavelengths has been identified similar to observations elsewhere (Alford *et al.*, 2016).

In the oligotrophic to ultra-oligotrophic Levant Basin, the nutricline does not overlap with the thermocline, notably with respect to nitrite and phosphate content (Kress & Herut, 2001; Krom *et al.*, 2005). Ongoing warming further increases the ecological stress in the upper water column (Sisma-Ventura *et al.*, 2014; Rilov, 2016; Ozer *et al.*, 2017). The low productivity leads to high light penetration, with the 1% photosynthetic available light depths in the pelagic and neritic domains being at ~109 ± 20 m (n = 21) and ~60 ± 20 m (n = 11), respectively (Berman *et al.*, 1984; Megard & Berman, 1989; Stambler, 2014). However, this figure varies with the season and meteorological events, such as dust

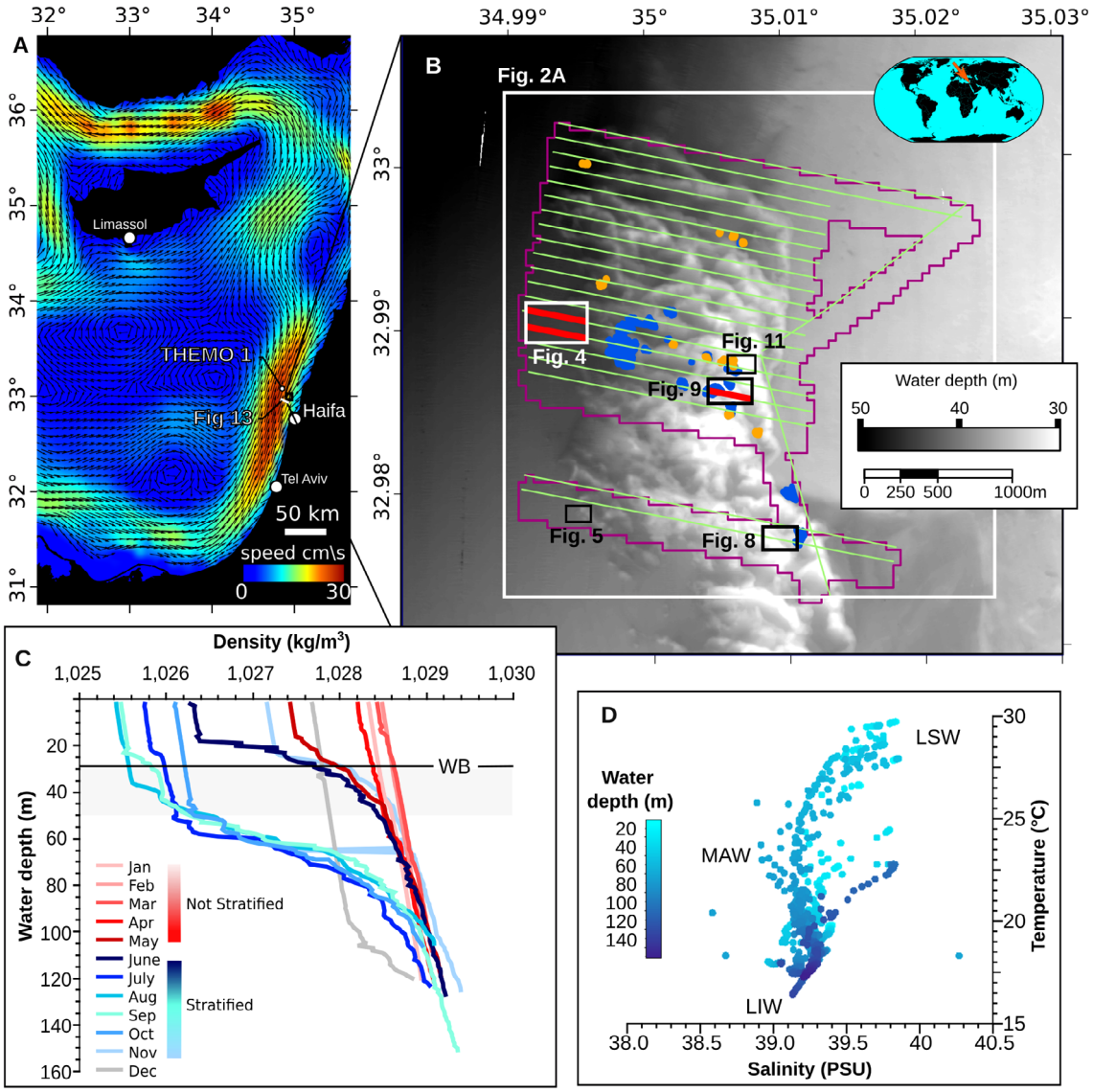

Fig. 1. (A) Modelled mean surface currents over 10 years (Global Ocean Physics Analysis and Forecast from the Copernicus network); Map of the Israeli and southern Lebanese shelf showing the position of the study area and location of the THEMO 1 observatory buoy, inset shows the location of this map relative to the globe. (B) Map of the study area, showing the overall bathymetry and location of Bustan HaGalil Ridge, areas of manual mapping of sediment bedforms and rocks (blue and orange, respectively), as well as the location of seismic lines (green); the purple polygon delineates the outer parameter of the AUV survey. (C) Annual variation in temperature at THEMO 1 in the top 150 m (data from Reich *et al.*, 2021), dark grey band outlines the annual amplitude of the pycnocline, light grey the depth distribution of sediment bedforms observed in this study, black line denotes the 99 percentile of effective wave depth which we consider as our wave base (WB). (D) Salinity/temperature for the top 150 m at THEMO 1. LIW, Levant intermediate waters; LSW, Levant surface waters; MAW, modified Atlantic waters.

storms that affect the region. Furthermore, rapidly increasing sea surface temperatures result in ongoing processes of species shift and 'Tropicalisation' in the coastal area of the Eastern Mediterranean (Bianchi & Morri, 2003; Rilov & Galil, 2009; Grossowicz *et al.*, 2020).

The 10 to 20 km wide Southeastern Mediterranean Sea continental shelf comprises the eastern

littoral cell of the Nile River, generally narrowing from south to north (Emery & Bentor, 1960). In general, the seafloor sediment grain size decreases significantly across the 30 m isobath, from fine sand to very fine sand with a significant clay and silt fraction (Almogi-Labin *et al.*, 2012). However, in the northern part of the Israeli shelf (north of ca. 32.6°N), at the edge of the Nilotic littoral cell (the main source of siliciclastic grains in the region), the coarser grain fraction increases and extends past the 40 m isobath. This region is characterised by a higher carbonate content of up to 47% (Almogi-Labin *et al.*, 2012), indicating a higher relative contribution of local sediment supply. Sets of generally shore-parallel ridges (locally referred to as Kurkar Ridges, beach ridges in some sources) stretch along the coastal zone and the middle shelf (~30 to 40 m water depth) of Israel (Almagor *et al.*, 2000). These underlying ridges have developed on land in the nearshore depositional environments, during different Pleistocene glacial cycles under the influence of the changing sea level and are aeolian ridges (Mauz *et al.*, 2013; Shtienberg *et al.*, 2017). The offshore ridges form one of the main hard substrates on the shelf and serve as the base of most offshore reefs in the region (Rilov *et al.*, 2018). They show a high biodiversity and are presently being overwhelmed by invasive species (Rilov, 2013; Peleg *et al.*, 2020). If similar to their present coastal equivalents, the underlying aeolianites are composed of a mixture of biogenic grains (molluscan aragonite and coralline algae high-Mg calcite) and lithogenic quartz (Porat *et al.*, 2003). These aeolianites are usually bound by two generations of cement—an early grain-coating micritic cement and a later pore-filling sparry cement.

Some of the most prominent aeolianite ridges are found on the shelf of northern Israel, including the study area of the Bustan HaGalil Ridge (Eytam & Ben-Avraham, 1992; Sade *et al.*, 2006; Fig. 1B). This is an elongated, up to 10 m tall, complex system of seafloor ridges. It extends for 7 km in the north–south direction and up to ~1.5 km in the east–west direction between water depths of 27 to 50 m. The Bustan HaGalil Ridge acts as a boundary between the soft (mostly silty) seafloor sediments to the west and mostly hard carbonaceous seafloor to the east. Habitat classification from the Bustan HaGalil Ridge revealed that this geomorphologically complex mesophotic environment supports a particularly diverse fish community (Sørensen *et al.*, 2025), highlighting its ecological significance in a regional context. The structural heterogeneity of the ridge likely enhances this richness (García-Charton & Pérez-Ruzafa, 2001), contributing to its role as a biodiversity hotspot. The area has also attracted local artisanal fishers, particularly those based in the nearby coastal city of Akko. As such, the ridge holds not only ecological importance but also socio-economic value, serving as a key resource for small-scale fisheries in the area.

MATERIALS AND METHODS

An ultra-high-resolution geophysical investigation of the seafloor environment of Bustan HaGalil Ridge (Figs 1B and 2) was carried out using the University of Haifa's ECA Robotics Inc. A18-UH deep-water surveying autonomous underwater vehicle (AUV) SNAPIR, operated off the R/V Bat-Galim from Israel Oceanographic and Limnological Research Institute. The AUV survey was carried out on 22 May 2019, acquiring a total of 47 km of hydroacoustic data over the northern half of Bustan HaGalil Ridge, at a flight elevation of 20 to 25 m above the seafloor in water depths of 25 to 50 m. Surveying involved data acquisition with: (1) a 337 kHz Kraken Robotics MINSAS120 Interferometric Synthetic Aperture Sonar (SAS), providing acoustic backscatter images with a swath width of 100 m to both sides and a resolution of 3 cm; (2) a Norbit WBMS 400 kHz multibeam echo sounder; (3) an Edgetech 2205 single channel Sub-Bottom Profiler (SBP) using a 2 to 10 kHz chirp signal with a vertical resolution of ~20 cm.

The Sub-Bottom Profiler (SBP) data were extracted as full-wave (Real) and were processed and interpreted using AspenTech SSE software suite (formally Paradigm). Following real-time application of the matching filter, the post-processing scheme involved a minimum entropy deconvolution, 7.5 kHz high-cut filter and amplitude scaling. Multibeam data were processed with QPS Qimera (version 2.6.2) and resulted in a 1 m bathymetric grid. Spatial features were processed and analysed in ESRI ArcGIS (Desktop version 10.8 and Pro) and QGIS (version 3.28). The multibeam bathymetry and SAS imagery were analysed to identify the changes in seafloor characteristics across the study area. An analysis of the bedforms was performed across three selected soft sediment-rich

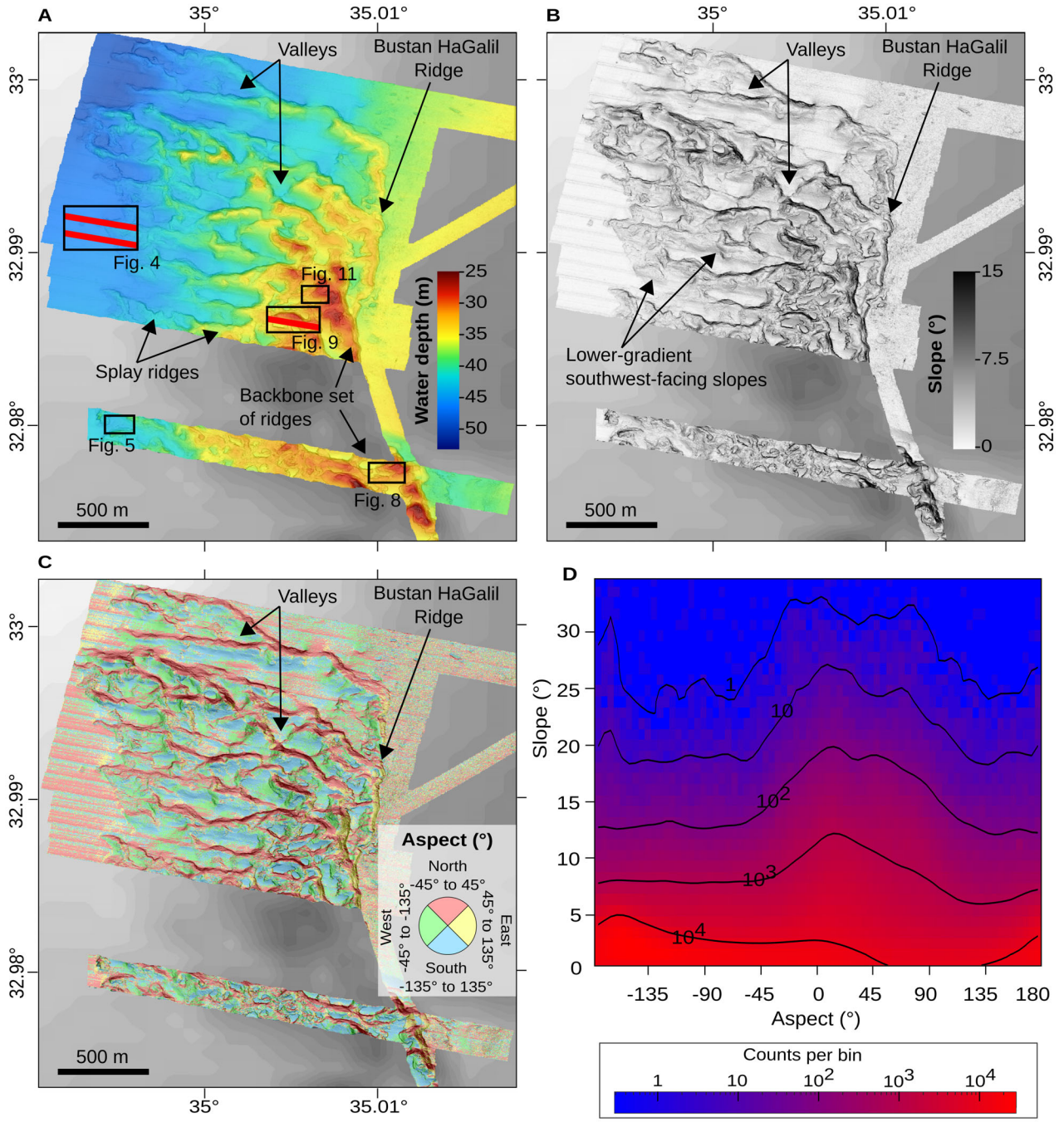

Fig. 2. Bathymetric properties of the surveyed area: (A) bathymetry; (B) slope angle; (C) aspect is divided into four coloured sectors for north, east, south and west with a 65% transparency and underlighting slope map in grey (as it is shown in B); (D) density plot of the relations between aspect and slope, higher slopes occur with a NNE aspect while lower slopes have a more southern aspect. Binning for the density plot is 1° for slope and 5° for aspect. On top are contours in black.

areas of interest located in the western, central and eastern part of the ridge; individual bedforms were manually identified and measured. Both starboard and port side imaging were compared (Appendix S1, Fig. S1.1) to verify that there was no bias from the illumination

direction. The survey was repeated with different illumination directions to compare the results and validate the measurements of the identified seafloor features. This is especially important for linear bedforms, such as ripples, sediment waves and dunes, as their appearance depends on the incidence angle (Appendix S1, Fig. S1.2). In total, the crest length and orientation of 8324 bedforms and the widths of 5143 bedforms were measured (Appendix S2, for complete list). Visualisation of statistical analysis was carried out using a combination of ArcGIS, MATLAB (MathWorks Inc., version 2022b), R software (R Core Team, 2024) with ggplot2 (Wickham, 2009) and QTIplot (Vasilief, 2010). In addition, 1053 rock features (small biogenic build-ups, see discussion below) were identified, and their size and distribution were also measured.

Sediment samples were collected via two dives using closed-circuit rebreather systems at depths of 30 m, where the SAS images were used for navigation. The divers also performed visual documentation of seafloor features which were used for ground truthing (Appendix S1, Fig. S1.3). In addition, quadrat images were collected to obtain a baseline understanding of the biogenic build-up across the ridge system. Four 25-m transects were surveyed, with one image taken every 2 m using a 25 cm × 25 cm photo-quadrat (13 images per transect). Transects were planned to represent habitat variation, with two on elevated rocky ridge areas and two adjacent to soft sediment zones in depths of 30 to 33 m. The quadrat was positioned perpendicular to the substrate to ensure consistent framing of benthic features. For sediment samples, the dive locations were selected based on the presence of all bedforms (see description of SAS findings in the Results chapter). In quadrat photographs, the three to four most visually dominant taxa were identified to the highest possible taxonomic resolution, generally to genus level. Names and terminologies for all taxa follow those on the WORMS database. The sediment samples were washed with fresh water and air-dried prior to microscopic analysis. Mineralogical analysis was carried out using a Rigaku MiniFlex XRD diffractometer. Grain size was evaluated using the collected samples and by image analysis using ImageJ (quadrat images) collected during the dive.

Surface wave and velocity data were obtained from the long-term THEMO 1 buoy (33.040°N; 34.950°E), located ~8 km north-west of the study area, and available from the THEMO project's website (http://themo.haifa.ac.il/) (Fig. 1A). Details of the processing of the surface wave data (following Allen, 1985; Clifton & Dingler, 1984) and the raw data are given in the Appendix S3. Brunt–Väisälä frequency was calculated based on density data (Fig. 1C) collected monthly in 2018 and 2019 next to the THEMO 1 buoy during research cruises described by Reich *et al.* (2021) and available through ISRAMAR (https://isramar.ocean.org.il/); values are included in cycles/h in Appendix S4. The data were processed and visualised using R Software and MATLAB. The multi-channel seismic profile showing data inside the water column (collected on 20.06.2016) was processed and interpreted using the AspenTech SSE software suite. The processing procedure included a high-pass filter, amplitude balance, and time stacking (using a moveout velocity of 1500 m/s). For converting Two Way Traveltime (TWT) into meters, a constant velocity of 1500 m/s was used. The Mercator Global Ocean Physics Analysis and Forecast model (1/12° resolution, from the Copernicus network) was used to evaluate current velocities on a wider spatial coverage (https://doi.org/10.48670/moi-00016).

RESULTS

Ridges and sedimentary features of the Bustan HaGalil region

Analysis of the bathymetry reveals that the Bustan HaGalil Ridge is composed of multiple ~1 to 1.5 km long, generally east–west oriented, rocky ridges that splay from a ~6 km long, generally north–south oriented, backbone set of rocky ridges (Fig. 1B). The ridge, in its entirety, dips to the west. High-resolution bathymetry of the northern part of the ridge shows that its eastern peaks reach water depths of ~25 mbpsl (meters below present sea level), ~10 m above the surrounding seafloor. Its western margins submerge into the mid-shelf sediment-covered seafloor which dip from a water depth of ~45 mbpsl at the ridge's south-western edge to 50 mbpsl at its north-western edge. The splay ridges are ~50 to 200 m wide (Fig. 2; Appendix S1, Fig. S1.4) with generally elongated east–west trending valleys located between them (Fig. 2D). The valleys are 100 to 500 m wide along their E-W axes and 50 to 100 m along their N-S axes. Some of the valleys are

enclosed by the splay ridges while others are open on their western side (Fig. 2A). The valley floors are shallowest in the east at ~35 mbpsl and generally deepening to ~45 mbpsl in the west.

The seafloor bathymetric gradients highlight the multi-scale variability of the seafloor morphology, with gradients of over 15° (<1% above 15°, some of which are suspected to be artefacts), and a mean gradient of 3.21° ± 3.10° (n = 4 461 091), reflecting the overall dip of the entire ridge and its major elements (Fig. 2D). At the tens-of-metre scale, the ridges are asymmetric, with wider lower gradient south-west-facing slopes and narrower, steeper north-east-facing slopes (Fig. 3). At this scale, high gradients (>5°) are associated with aspects ranging between −30° and +60° (Fig. 2D) with the highest gradients appearing at the north-east-facing slopes (Fig. 2D). The north-east-facing slopes of the splay ridges terminate sharply (gradient >10°) at their bases (Fig. 3). At this scale, the ridge topography of the north-east-facing slopes appears smoother than that of the south-west-facing slopes (Fig. 3). Particularly in the south-eastern part of the study area, the soft sediment in the valleys is bounded by a small 0.5 to 1 m tall step or very steep slope (~30°) (Figs 2B and 3A). The size of this step is smaller or disappears towards the northern side of the valley (Figs 2B and 3A). The valley floors between the splay ridges and part of the southern side of the splay ridges are characterised by variable bedforms observed in the SAS data, which are described in detail in section 'Bedforms of the Bustan HaGalil Region'.

Two types of mesophotic reef elements are distinguished within the Bustan HaGalil Ridge. Continuous rocky elements with their long axis >10 m and a distinct relief are referred to as 'ridges/reefs'. Similarly, any continuous solid mass with its longer axis ≤10 m that is also spatially separate from any other rocky mass is defined as a solitary reef/bioconstruction. This delineation is based on the observed dimensions of the non-continuous rock masses in the study area.

In SBP profiles, the Bustan HaGalil Ridge bedrock is characterised by high-amplitude, high-frequency, disrupted to chaotic reflections. In contrast, continuous layered, medium to low amplitude reflections represent the sedimentary cover above the bedrock. The SBP data reveal that the main Bustan HaGalil Ridge bedrock structure is buried at its periphery by decimetres-thick layered sediments, with their thickness increasing up to several metres away from the main ridge (Fig. 4). Some of the buried ridge peaks outcrop on the present seafloor as solitary rocky elements. The bathymetric data show that north–south orientated elongated depressions formed adjacent to the western edges of the splay ridges (e.g. Fig. 4A), with mounded morphologies located next to these depressions. These are identified as moats with adjacent separated mounded drifts (Fig. 4C). The SBP profiles show continuous seismic reflections extending from the moat to the drift, classifying it as a so-called constructional moat-drift

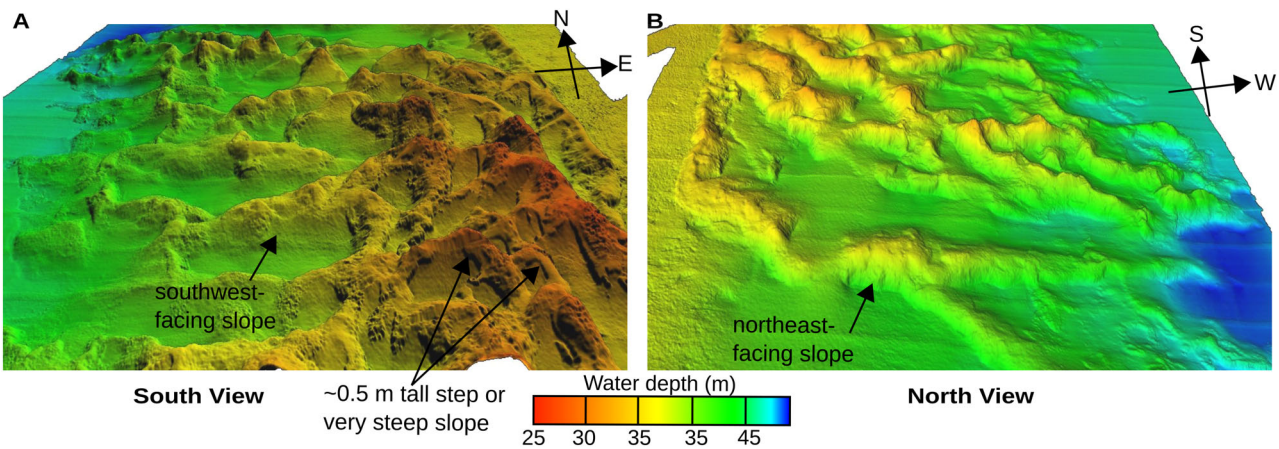

Fig. 3. 3D shaded relief views (VE = 8.5, light direction: altitude 45, Azimuth 45) of the Bustan HaGalil Ridge: (A) from a south perspective and (B) from a north perspective, demonstrating the asymmetric nature of the features.

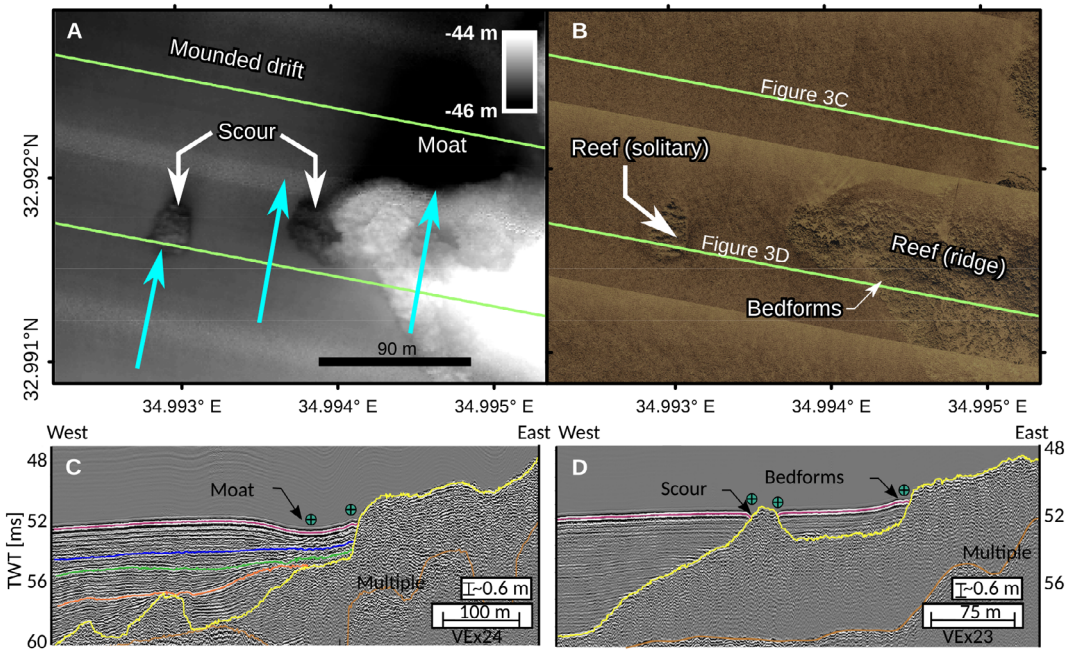

Fig. 4. Character of the sediment on the western flank of the Bustan HaGalil Ridge. (A) Bathymetric and (B) SAS image. Green lines show the location of the seismic lines, and blue arrows indicate the direction of the main current. (C) Interpreted seismic imaging showing the northern line. (D) Interpreted seismic imaging showing the southern line.

system. The layered sediments exhibit onlap patterns (Fig. 4C). Evidence for scouring also appears in the SBP data, showing distorted and mounded layering in the vicinity of some of the ridges' promontories/solitary reefs (Fig. 4B and C). These appear in the uppermost (youngest) layers, as well as in some of the deeper (older) reflections.

Bedforms of the Bustan HaGalil region

SAS data reveal multiple bedforms inside the valleys (Fig. 5). The types, sizes and directions of the bedforms change spatially within the valleys. Some bedforms are only visible with the SAS and cannot be distinguished at the resolution of the multibeam bathymetry (Appendix S1, Fig. S1.5). Consequently, their relief is unknown.

The SAS data show that bedforms occur in three principal types: large linear bedforms that look like dunes (Fig. 6D), short chevron bedforms that show a zigzag-like or v-shaped pattern (Fig. 6E), and superposition of the two (Fig. 6F). Analysis of the manually traced bedforms (n = 8325, Fig. 1B) ranges in axis lengths from ~0.3 m to 70 m and wavelength from ~0.2 m up to 7 m, with the 10th to 90th percentile ranging between 0.6 and 1.9 m, respectively (Fig. 7A). The linear bedforms are aligned primarily with a north–south bearing axis. Measurements reveal that these bedforms reach up to 70 m along their long axis (Fig. 7B) and, for the most part, exhibit a maximum wavelength of up to 2 m. The chevron bedforms are shorter, with a north-west–south-east or north-east–south-west axis orientation (Fig. 7C). Sometimes, chevron bedforms are superimposed on the linear bedforms (Fig. 6F); whereas, in a few cases, they occur as poorly developed ladder-like bedforms (small bedforms linking adjacent larger ones) in between the linear bedforms. The chevron bedforms extend to a maximum length of ~15 m and have a wavelength of up to 7 m. The bedforms are generally concentrated in stretches along the valleys and up the southward-facing slopes of the ridges (Figs 8 and 9A). There seems to be a decrease in wavelength (from 2.5 to 0.5 m) from the southern part of the valley to the north (Fig. 8), but this was not observed consistently across the study area. The linear bedforms occur primarily in the southern part of the valley, while the chevron bedform occurs primarily in the northern part (Fig. 9A). However, the chevron and mixed

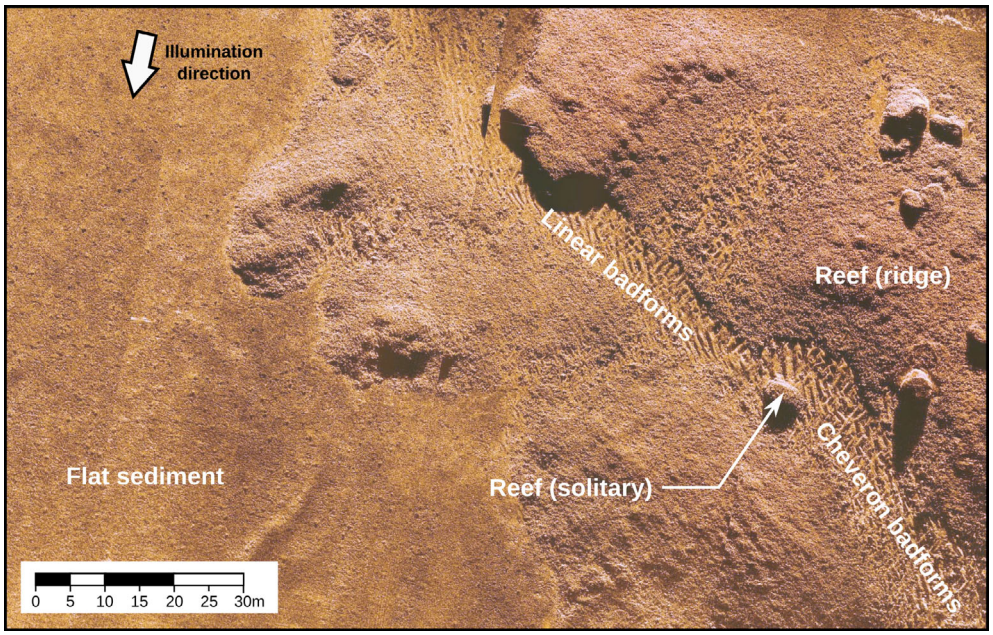

Fig. 5. Wide-scope mosaic of the SAS imaging in the western margin of the survey area showing the three main seafloor types in the study area. See Fig. 2 for location.

bedforms can also occur in the south of the valleys, but there they are very small (below 2 m along their long axis, and wavelength below 2 m). The SBP profiles reveal that transitions between chevron and linear bedforms coincide with an increase in sediment thickness (Fig. 9B and C). The chevron bedforms are present where the sediment layer is thinner, while the linear bedforms correspond to a thicker layer of sediment in the valleys. There is no clear correlation between the wavelengths and bedform axis lengths ($r = \leq 0.19$, $n = 5143$; Fig. 7D) nor with the bearing ($r = -0.01$, $n = 5143$ and $r = 0.01$, $n = 8324$, respectively). However, the relation between bedform wavelengths and bedform axis lengths shows two trends (with a gradient between them): a long axis/short wavelength cluster, which is mainly associated with linear bedforms, and a long wavelength/short axis cluster, which is mainly associated with chevron bedforms.

Solitary reefs

Analysis of the bathymetry and SAS data reveals that the solitary reefs/bioconstructions occur in two main forms—adjacent to a ridge (Figs 5 and 6A), or scattered between bedforms regardless of any ridge (Fig. 6B and C), with the former often observed to be larger in size. The solitary reefs/bioconstructions vary from coarse gravel to boulder sizes (on the Wentworth, 1922 scale) and are observed to occur in the trough between bedforms or at the endpoint of bedforms. Adjacent to boulder size rocks/bioconstructions, a change in bedform character or direction is sometimes observed. The majority of rocky elements range from 0.13 to 20 m along their long axis; the size distribution is highly skewed ($\mu_3 = 5.2$, $n = 1053$; Fig. 10) and >50% of the rocky elements are under 0.76 m in length. Thus, around half of the rocky elements are classified as maerl (rhodoliths) and, as such, mobile (Hottinger, 1983). The larger rocks/bioconstructions and ridges/reefs show a crinkly texture, and in some places, individual branches (possibly of coralline algae or bryozoans) can be identified in the SAS images (Appendix S1, Fig. S1.6), suggesting extensive biofouling of all available substrate.

Seafloor coverage and sedimentary description

Visual inspection by divers of both the rocks/ridges and bedforms (Fig. 11A) reveals extensive

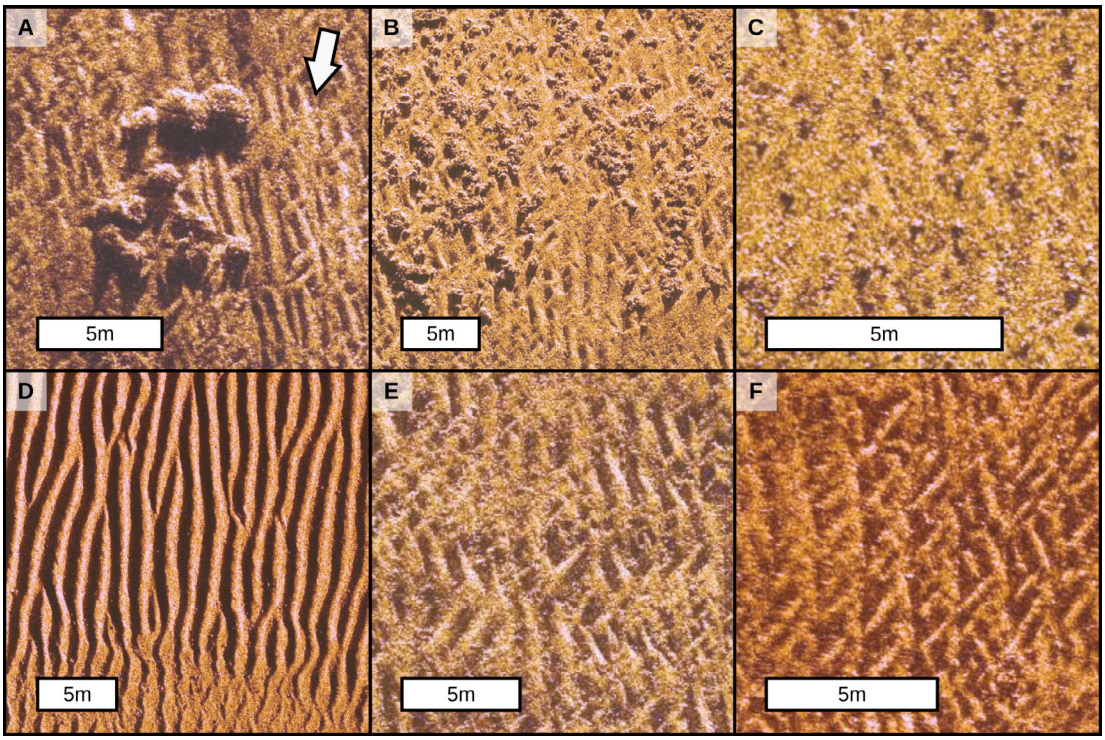

Fig. 6. Representative SAS imaging of the seafloor features: (A) large solitary bioconstruction (boulder size); (B) intermediate constructions; (C) small bioconstruction or rocks, suspected rhodolites; (D) linear bedforms; (E) chevron bedforms; (F) superposition of chevron bedforms on top of linear bedforms. All scale bars are 5 m; the arrow in (A) shows the illumination direction.

biogenic cover over the rocks (Fig. 11B). A total of 54 images (e.g. Appendix S1, Fig. S1.3) from the ridge were analysed to characterise the biological cover. The most abundant phylum by counts (Table 1) is Rhodophyta (red algae), followed by Hydrozoa (hydroids), Chlorophyta and Porifera. Commonly observed genera included *Rhodymenia*, *Lithophyllum*, *Lophocladia* and *Jania* (Rhodophyta); *Caulerpa* and *Cladophora* (Chlorophyta); *Crambe*, *Axinella* and *Ircinia* (Porifera). A relatively high occurrence of encrusting *Lithophyllum* sp. was noted, particularly in areas where algal overgrowth was limited. Additional taxa included members of Bryozoa (e.g. branching forms, *Phobas*), Phaeophyceae (e.g. *Padina*) and ascidians from Chordata (e.g. *Didemnum*). Epiphytic large benthic foraminifera were also frequently observed across the images. Based on analysis of the dive photography and the SAS data, the seafloor in the Bustan HaGalil Ridge region can be divided into three main substrate forms: reef/bioconstructions (reefs, rhodoliths, other calcareous nodules, etc.), bedforms and a near-flat sediment surface. In contrast to the layered sediments around the Bustan HaGalil Ridge, the bedform patches within the Ridge's valleys, visible in SBP profiles, comprise a relatively thin sedimentary layer overlying the bedrock (Fig. 9). The maximum thickness of the sediment is ~0.6 m (~0.5 m assuming a velocity of 1500 m/s).

The loose sediment samples collected by the divers comprise primarily calcareous grains ranging in sizes from coarse sand to coarse gravel (calcarenite to calcirudite *sensu* Grabau, 1904) with a major portion identified as fine to medium gravel (Fig. 11C and D). The dive photographs of the bedforms area reveal that coarser grain sizes mainly occur in the troughs and finer grain sizes at the crests of the bedforms (Fig. 11C). The grains are composed primarily of small coralline algae nodules with other bioclastic fragments a few millimetre to centimetre in size (Fig. 11D and E; Appendix S1, Fig. S1.3). The nodules are brown, black or yellowish red, rounded, elongating or irregular in shape, ranging in size between a few millimetre and a few centimetre. Most of the

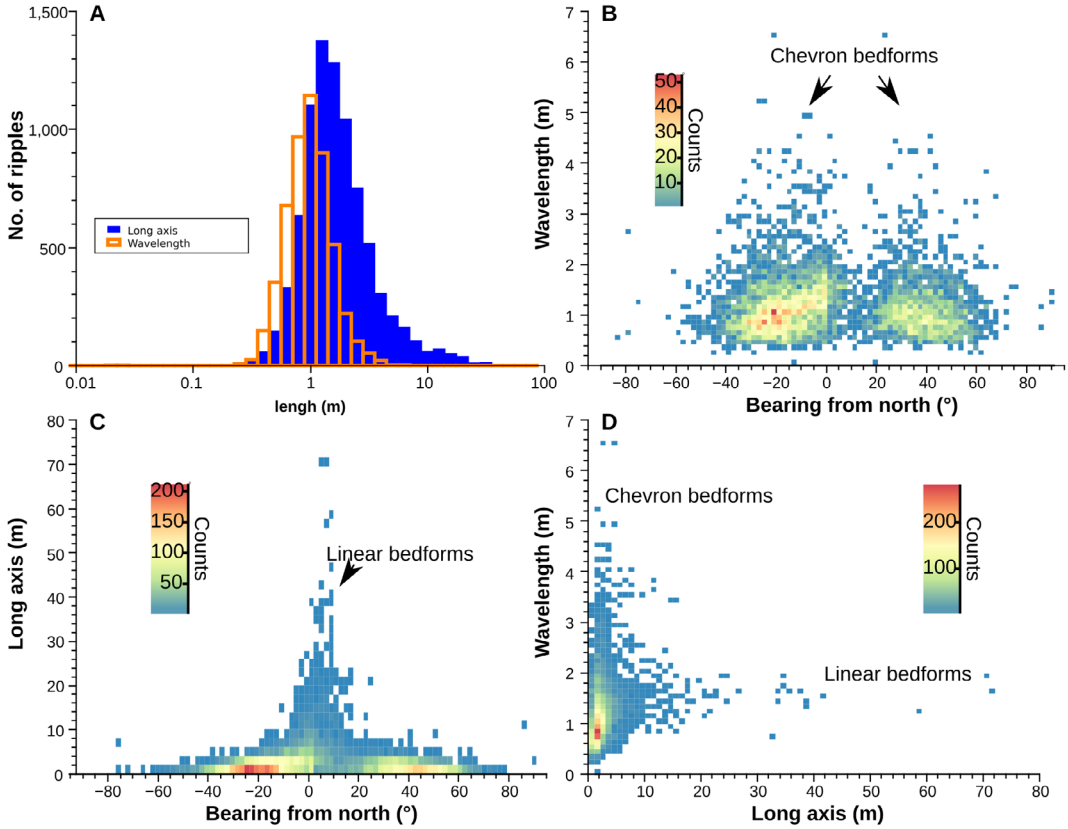

Fig. 7. Bedform characteristics: (A) distribution of long axis length (n = 8323) and bedform wavelength (n = 3557); (B) relation between bearing and wavelength; (C) relation between long axis length and bearing; (D) relation between wavelength and long axis length.

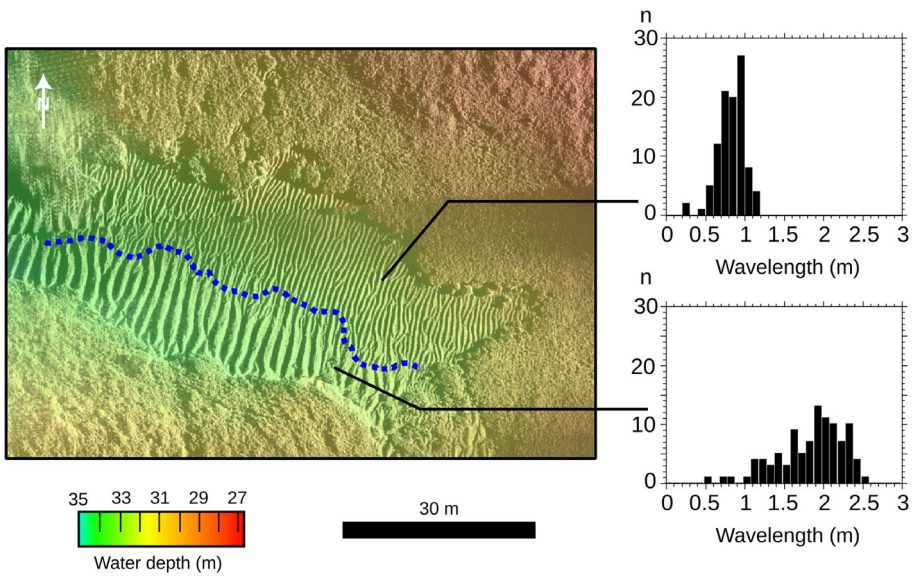

Fig. 8. Relation between bathymetry and bedform morphology. Interlaced seafloor SAS seafloor image and bathymetry (note: slope is steeper south of the line), blue dashed line marks the transition between bedform morphologies. Histograms (n = 100) show the change in wavelength on either side of the dashed blue line. See Fig. 2 for location.

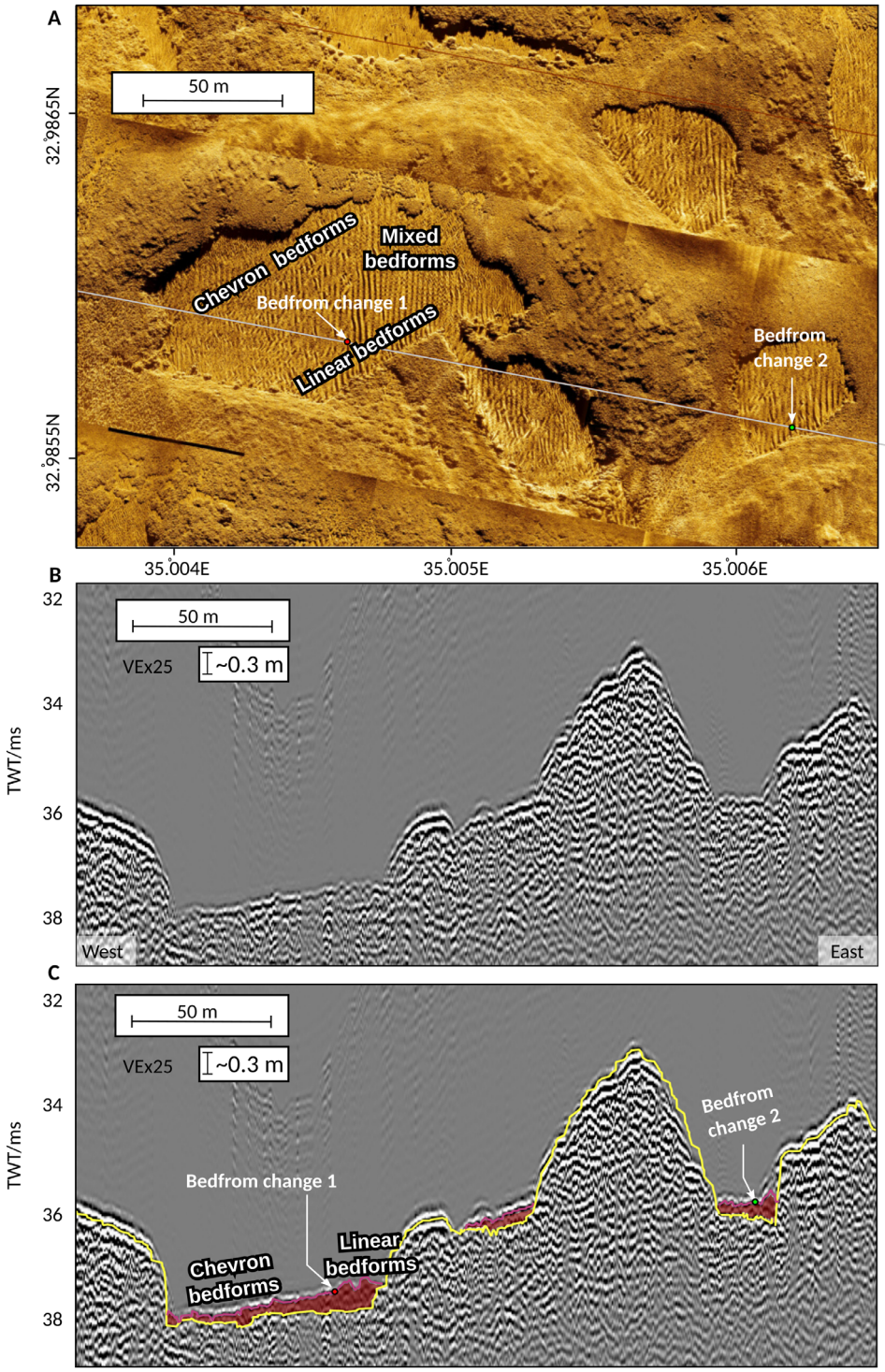

Fig. 9. Seismic line across the sedimentary fill of the valleys. (A) SAS imaging of the seafloor along the seismic line, the transition from chevron to linear bedforms is marked. (B) Uninterpreted seismic imaging. (C) Interpreted seismic imaging showing the sedimentary fill (red) and the top of the rock surface (yellow). See Fig. 2 for location.

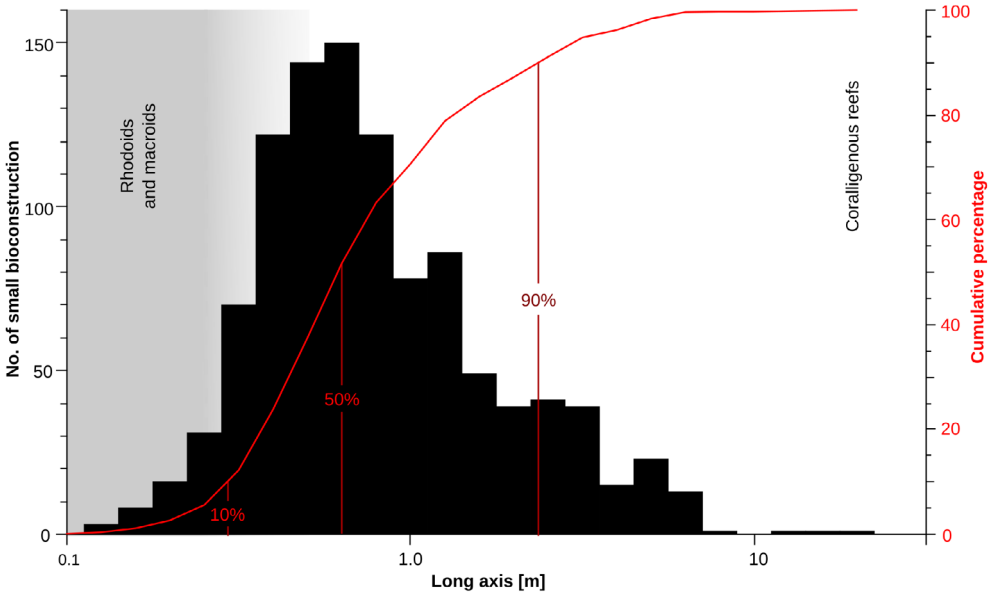

Fig. 10. Long-axis size distribution (log scale) of rocks/bioconstructions sampled from the SAS imaging (n = 1053); vertical lines denote the percentile fractions.

coralline algae in the nodules appear to be dead, based on colour and the presence of encrustation on some of the nodules. The encrustations are mainly formed by bryozoans, although serpulids or other vermiforms are observed as well as possibly some encrusting foraminifera (*Miniacina sp.* or *Homotrema sp.*). The bioclastic fragments include bivalves, gastropods, serpulids (or vermetid), echinoderms and bryozoans; individual coral polyps were also found. Bryozoan fragments of multiple morphologies, including branching and encrusting forms, are common. A few larger benthic foraminifera are present, mainly the invasive species *Amphistegina sp.*

Local wind and surface wave character

The surface waves on the Galilee shelf, measured by the THEMO 1 buoy, exhibit log-normal distributions of both the dominant period and significant wave height, with a log mean of 0.7 ± 0.2 (4.8 m) and −0.3 ± 0.3 (0.5 m), respectively (n = 18 841 for both). In contrast, the distribution of the mean period is closer to normal, with a mean of 3.7 ± 0.7 s. Calculating the wavelength from the mean period (Fig. 12, Appendix S5) results in a mean wavelength of 21.4 ± 9.6 m (n = 18 686, 487 days across 2019 and 2020) and a μ_3 = 1.8, the 10th percentile of 13.9 m, the 90th percentile of 35.4 m and a maximum wavelength of 84 m. This translates to a wave base shallower than 18 m for more than 90% of waves and only 1% reaching the depths of the sediment bedforms in the study area.

Water column characteristics

The calculated Brunt–Väisälä frequency distribution exhibits low values (1.6 ± 2.3 cycles/h, μ_3 = 1.2, n = 563) during winter and spring months (December to April) (Fig. 13). In the summer and autumn months (May to October), the values increase (5.9 ± 5.5 cycles/h, μ_3 = 0.5, n = 851). The highest frequencies (>25 cycles/h) are located between 20 and 80 mbsl, with two main peaks (Fig. 13) at 20 to 30 mbsl and 60 to 70 mbsl. High frequencies persist between these two peaks, which represent the migration of the pycnocline through the warm summer–autumn periods (Fig. 1C). These values and distribution are comparable to previously published values for the southern Israeli shelf (Reiche *et al.*, 2018). The high-resolution seismic sparker survey, acquired during the summer period (on 20.06.2016), imaged wavy, semi-continuous high-amplitude reflections at water depths between 30 and 50 mbsl (Fig. 13). These wavy reflections appear similar to internal waves. The internal waves exhibit wavelengths in the range

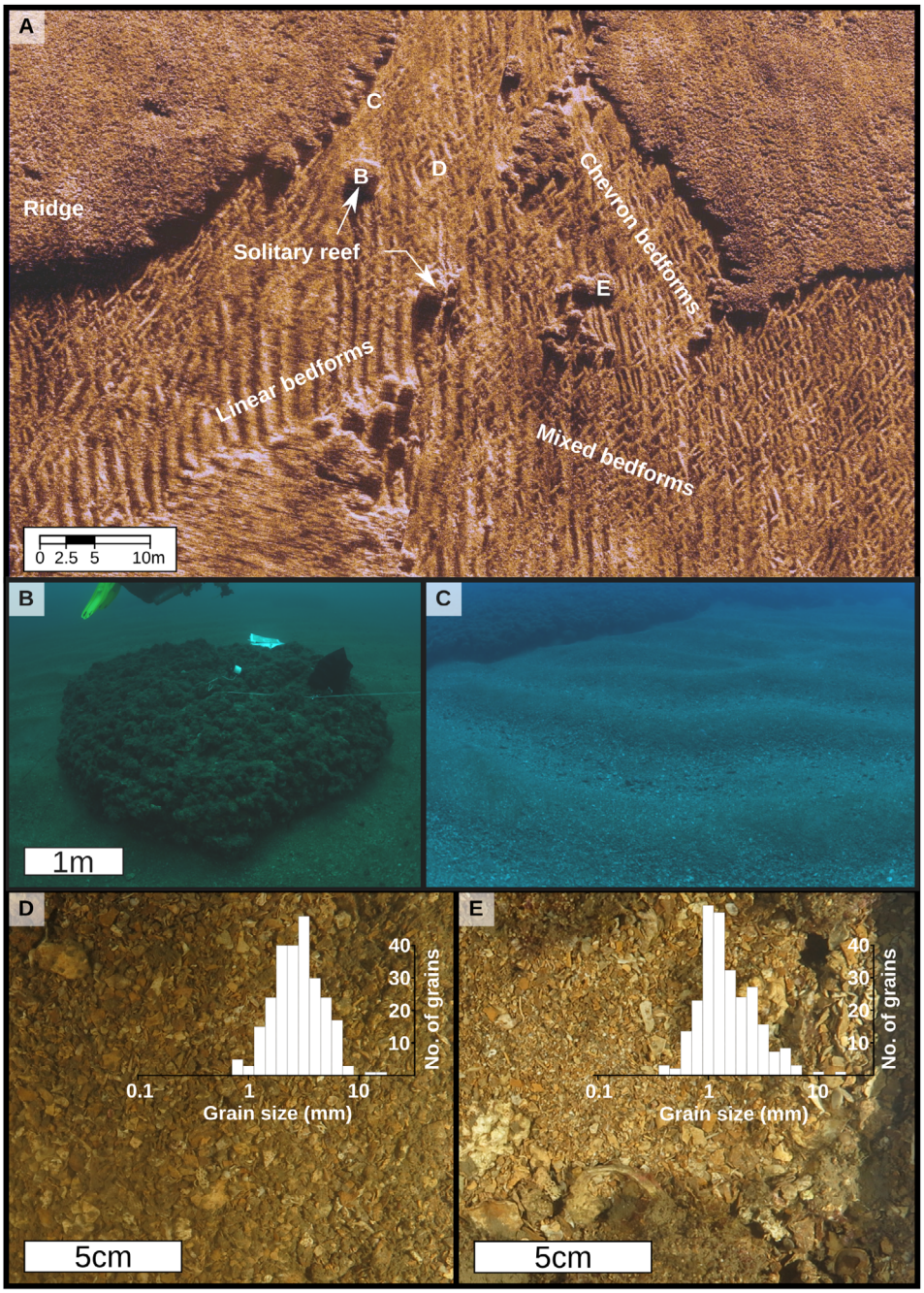

Fig. 11. (A) Configuration of bedform elements within a small valley, showing all types of bedforms and the location of subsequent subfigures. (B) Solitary reef/bioconstruction of encrusting organisms, notably coralline algae. (C) Individual bedforms at the base of the ridge. (D) Sediment and grain size distribution for the mixed bedforms. (E) Sediment and grain size distribution in the chevron bedforms. See Fig. 2 for location.

of 10 s of metres and a metre-scale amplitude (Fig. 13).

Surface currents measured over 1 year at THEMO 1 have an average velocity of 21 cm/s with a standard deviation of 15 cm/s (Fig. 14). Peak velocity is over 60 cm/s, and the main current direction is north to north-east. Based on the Global Ocean Physics Analysis and Forecast model from the Copernicus network, it appears that the THEMO 1 buoy is located in the centre

of a main NNE flowing along-slope current. The Bustan HaGalil Ridge is also inside the same main current but more towards its eastern boundary (Fig. 1).

Table 1. Occurrence counts of taxa along a 25 m transect on a ridge (hard substrate) in the Bustan HaGalil Ridge (north of point C in Fig. 10A).

Phylum	Representative groups/ genera	Total count
Rhodophyta	*Rhodymenia, Lithophyllum, Lophocladia, Jania, Halymenia*	50
Cnidaria	Hydrozoa (hydroids)	29
Chlorophyta	*Caulerpa, Cladophora*	23
Bryozoa	Branching forms, *Phobras*	21
Porifera	*Crambe, Axinella, Ircinia*	18
Phaeophyceae	*Padina*	6
Chordata	*Didemnum* (*Ascidiacea*)	6
Echinodermata	Sea cucumber	1

DISCUSSION

Biogenic structure

The Bustan HaGalil Ridge is a rocky structure on the northern Israeli shelf. The elevated parts of this structure offer hard substrates for the settling of various calcifying groups present in the Eastern Mediterranean. These include coralline algae, hydrozoans, bryozoans, sponges, larger benthic foraminifera, molluscs and potentially some corals (Idan *et al.*, 2018; Cerrano *et al.*, 2019; Corriero *et al.*, 2019; Albano *et al.*, 2020; Goren *et al.*, 2021). Remains of many of these groups also occur in the sediment found in the submarine valleys of the Bustan HaGalil Ridge (Fig. 11B to E). The binding, encrustation and accumulation of these organisms result in the development of extensive coralligenous bioconstructions. Thus, the Bustan HaGalil Ridge is similar to other mesophotic reefs (also referred to as biogenic build-ups) in the central Mediterranean Sea (Ingrosso *et al.*, 2018; Bialik *et al.*, 2022). The broad geometry of the Bustan HaGalil Ridge is similar to other Kurkar ridges at the coast and offshore Israel (Neev *et al.*, 1987). In the central Mediterranean, these ridges are strongly influenced by

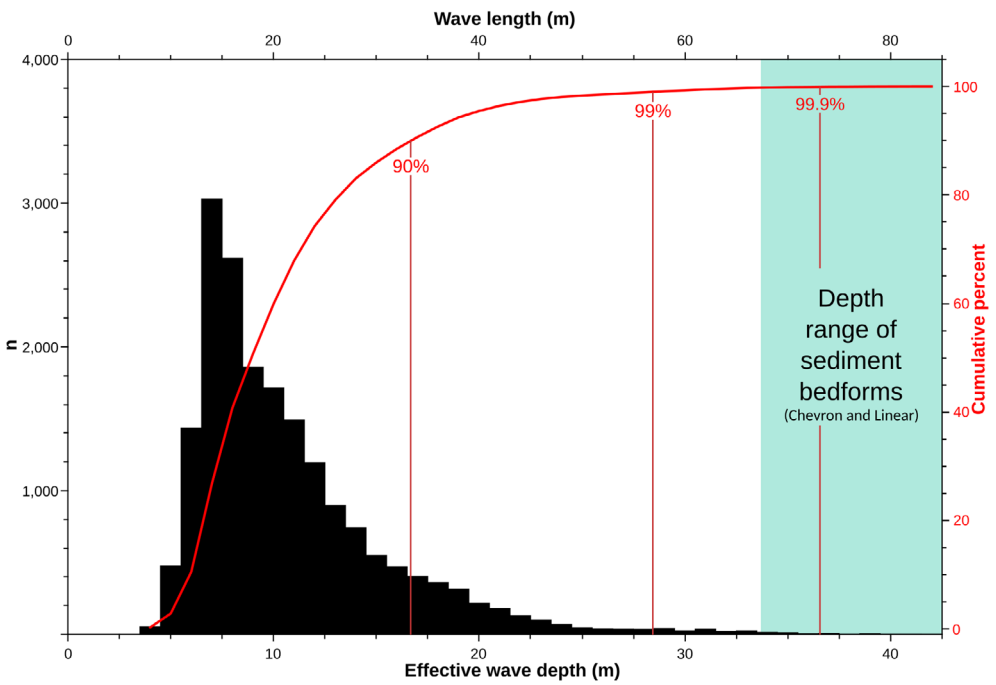

Fig. 12. Wavelength distribution based on the THEMO 1 data, blue area marks the affected depth range in the study area.

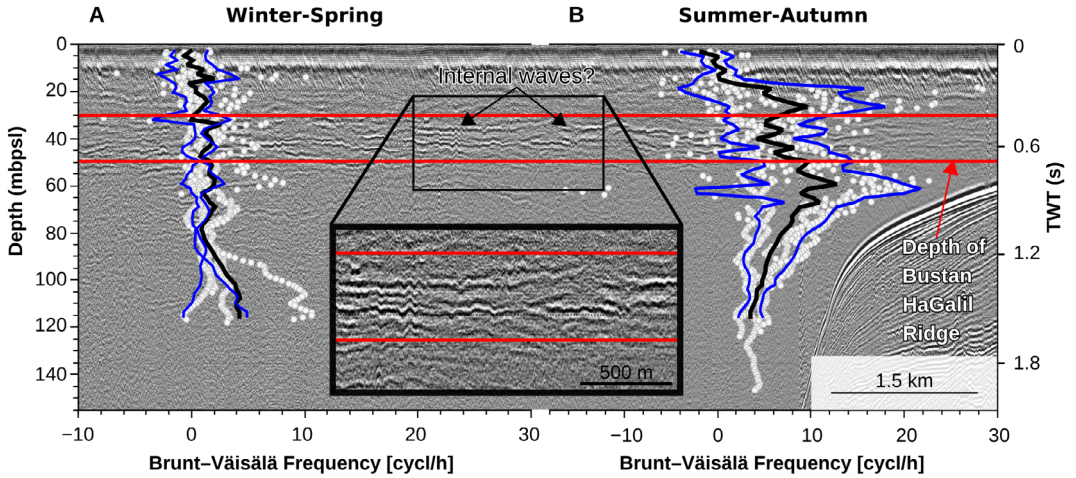

Fig. 13. Distribution of Brunt–Väisälä frequencies in the water column during winter–spring and summer-autumn (see Fig. 1C for density distribution over each month). The half-transparent background shows imaging of the water column with multi-channel seismics. This possibly shows internal waves between 30 and 50 m water depth, which is also the depth between the two peaks in the Brunt–Väisälä frequency.

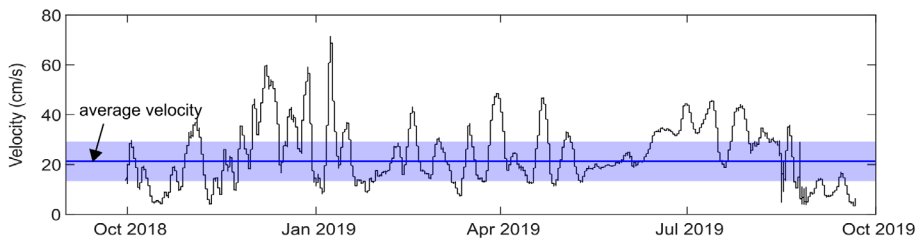

Fig. 14. Near-surface current velocity measured at THEMO 1 over a 1-year (average 21 cm/s with a standard deviation of 15 cm/s). See Fig. 1A for location.

the underlying Pleistocene strata (Varzi *et al.*, 2023), as is likely the case here. However, the development of the biological cover and build-ups is usually also controlled by local oceanographic conditions. Currents are most likely an important mechanism to transport nutrients, which leads to differential biogenic growth rates on the southern and northern sides of the ridges. Most Pleistocene beach ridges in the region are north–south oriented (Mauz *et al.*, 2013), whereas the smaller splay ridges of the Bustan HaGalil Ridge are oriented in an east–west direction (Fig. 2D). This suggests that the modern structure evolved subaqueously through interactions of oceanographic and biological processes.

The coralligenous biogenic grains, resembling those in the build-ups, suggest that sedimentary patches between ridges derive from nearby reefs. The production of most of these components probably occurs predominantly on the higher areas and is then transported to the valleys by currents and gravity. Based on the size distribution (Fig. 10) of the smaller rocky elements found on the sediment patches, and the prior description of large rhodoliths in this region of the Israeli shelf (Dulin *et al.*, 2020), they are identified here as rhodoliths (Fig. 6C). In difference to the other fragments, some coralline algae nodules in the sediment appear to keep growing. When coralline algae fragments break off from mobile substrates, they can form nodules as currents and animals move them around (Braga & Martín, 1988). The production of calcium carbonate is most likely local and limited due to the high stress and low nutrient availability in the region (Krom *et al.*, 2005;

Thingstad *et al.*, 2005; Ozer *et al.*, 2017). The limited production potential presumably explains the relatively thin sediment layer of the relief/valleys between the ridges (Fig. 8C).

Another mechanism which influences grain generation and distribution is bioerosion and resuspension by fish (Katz *et al.*, 2012). The rocky reefs of the region have experienced a large-scale invasion of Indo-Pacific biota from the Red Sea through the Suez Channel, referred to as Lessepsian species (Edelist *et al.*, 2013; Rilov *et al.*, 2018; Ofir *et al.*, 2023). Species such as the rabbit fishes *Siganus rividae* and *S. luridus* have led to a paradigm shift in the benthic macroalgae community, thereby affecting the overall ecosystem (Sala *et al.*, 2011; Rilov *et al.*, 2018). Although less abundant than in shallow waters, these herbivores are still present in reefs down to 45 m depth (https://haifauniversity.shinyapps.io/FishsurveyApp2/). Other species such as *Scarus ghobban* and *Parupeneus forsskali* also contribute significantly to the bioerosion and resuspension; in their native regions of the Red Sea (Yahel *et al.*, 2002; Alwany *et al.*, 2009), these are suspected to be affecting the Bustan HaGalil Ridge as they are present in the region. Although little is known of their effect on the redistribution of biotic and abiotic components in the Mediterranean rocky reef setting, these organisms likely function as ecosystem engineers. Their presence probably affects sediment composition and grain size in the sediment patches between the ridges.

Mesophotic reefs are usually not affected by fair-weather waves' resuspension (Baker *et al.*, 2016). Lateral transport is of greater importance in mesophotic settings than deposition from the water column (Sherman *et al.*, 2016). This redistribution of material impacts the lateral and vertical growth of the reef, as well as the ecosystem that inhabits it, similar to shallow water reefs (Storlazzi *et al.*, 2004; Hernández *et al.*, 2009). An extensive evaluation of surface waves shows that <1% of surface waves affect the sediment in the Bustan HaGalil region (Fig. 12). Yet, when accounting for the relatively large grain size (Fig. 11D and E) and maximum wave height (Appendix S5), most of these waves would not be able to agitate the sediments in the valleys (Flemming, 2024).

Regional along-slope current

To understand the sediment dynamics in the study area (discussed in the next section), the regional along-slope current dynamics and its potential to transport sediment must be evaluated. For the analyses of the current dynamics, a combined approach of large-scale and long-term modelling and local measurements is used. The model indicates a generally northward flowing along-slope current, and the local measurements show average current speeds of 21 cm/s with peak velocities over 60 cm/s at the sea surface. The observed asymmetry of the splay ridges suggests that bottom currents are strong enough to transport sediment to the north. This sediment transport appears to be blocked by the splay ridges (oriented west to east), resulting in the sediments piling up at the south-west-facing side of the ridges. This means that the sediment distribution in the valleys is asymmetric, with more sediment accumulating in the northern part. The sediment transport in the valleys towards the north explains the lower gradient of the south-west-facing side of the splay ridges. Thus, the sediment located in the valleys is mainly transported as bedload and cannot cross over the ridge, unlike suspended sediment in the water column. Currents that are strong enough to resuspend sediment flowing next to a slope or an obstacle like a reef commonly lead to the formation of moats (Faugères *et al.*, 1999; Nielsen *et al.*, 2009; Paulat *et al.*, 2019; Miramontes *et al.*, 2021; Wilckens *et al.*, 2023). This is in agreement with our observation of a moat and adjacent separate mounded drift next to the Bustan HaGalil Ridge (Fig. 4). Furthermore, the observed concentration of larger grain sizes is likely the result of winnowing of smaller grain sizes, which in other mesophotic systems appears to be related to currents (Bialik *et al.*, 2024). In general, the north-east-facing side of the ridges appears smoother. This is most likely related to winnowing of the smaller grain sizes that are resuspended and then deposited in the lee side of the ridges (meaning the north-east-facing side). Thus, the combined observations—including a strong south-to-north current, pronounced north–south oriented ridge asymmetry and the presence of larger grain sizes and moat-drift systems adjacent to the ridge—highlight the significant influence of the regional along-slope current on sediment dynamics at Bustan HaGalil Ridge.

Bedform development

The bedforms are located in the sediment patches in the valleys between the ridges and

are large linear bedforms showing a wavy sediment structure (hereafter referred to as 'dunes') and chevron bedforms that show a zigzag-like or v-shaped pattern. The terminologies of megaripple, sediment wave, sand wave and dune have been used differently depending on the disciplines and researchers (Nanson *et al.*, 2023). Here we follow the recommendation to use the term dune (Ashley, 1990). In general, dunes can be created by oceanic along-slope currents, surface waves and internal waves (Wynn & Stow, 2002; Miramontes *et al.*, 2020, 2021). Thus, we evaluate each of these mechanisms for their potential to generate the observed linear bedforms.

Along-slope currents

To form sediment waves, ripples and dunes, the along-slope current velocity has to be in a specific speed interval that depends on the sediment grain size according to the bedform velocity matrix (Stow *et al.*, 2009). As the previous discussion about the current dynamics in the study area has indicated, the currents are strong enough to move the sediment northward, leading to the asymmetry of the splay ridges and the development of a moat-drift system. Sediment waves, ripples and dunes created by along-slope currents are usually orthogonal or oblique to the current flow direction (Wynn & Stow, 2002). The oblique direction is related to the three-dimensional Coriolis vector (Hopfauf *et al.*, 2001). Sediment waves can also be almost parallel to the flow direction; however, on a relatively flat seafloor, they are more or less perpendicular to the current direction (Faugères & Mulder, 2011). The combined analyses of modelled surface currents flowing northward together with the observed splay ridge asymmetry and moat-drift system all indicate a northward bottom-current flow in the study area. This is well in line with previous direct and indirect evidence for northward sediment transport near the study area (Golik, 1993; Katz & Crouvi, 2018). The observed north–south trends of the dunes appear to align with the directions of the bottom current and are located on a relatively flat seafloor. Thus, the bedforms are likely not created by a northward flowing bottom current. Possibly, the structure of the reef could influence the direction of the bottom current, causing it to flow around the ridges. In the absence of current measurements close to the seafloor, it is not possible to examine this mechanism. However, such a mechanism, if it occurred, would still fail to explain why the sediment waves are aligned north–south (meaning with the regional along-slope current) (Fig. 7C) in areas that are enclosed by the reef structure (Fig. 9). Splay ridge asymmetry indicates predominantly northward along-slope bottom currents throughout the study area. This northward flow cannot explain the north–south dune orientation and is therefore not considered the primary formation mechanism.

Surface waves

As the along-slope current alone cannot explain the bedforms' orientation, an oscillatory flow is necessary to create such kind of wave structures. Surface waves are one possibility for such an oscillatory flow. However, since no more than 1% of the surface waves reach the depths of the sediment bedforms (Fig. 12), it is unlikely that they could be the primary mechanism responsible for their formation. The fact that the sediment is not consolidated suggests continued agitation which prevents cementation (Braithwaite *et al.*, 2000). Yet, the absence of common tracks or other traces of bioturbation suggests that this agitation is not caused by metazoans.

Internal waves

An alternative to surface waves is internal waves that can propagate on density boundaries inside the water column (Talley *et al.*, 2011). Mooring data from the DeepLev station (33.0612°N; 34.488°E), located ~50 km away from the study area, show the frequency spectra of internal waves (Solodoch *et al.*, 2023). In this study, internal waves are imaged at the pycnocline. The pycnocline is not static but oscillates in depth and intensity throughout the year. It therefore may generate multiple energy states that interact with the seafloor. The Brunt–Väisälä frequency, which is calculated based on salinity and temperature data (Fig. 13), indicates that internal waves can propagate in the depth range at which the examined bedforms occur, with a maximum frequency of, on average, 1.6 to 5.9 cycles/h (or a period of 10 to 37.5 min), depending on the season. It is important to note that these are the maximum frequencies for these conditions, and smaller frequencies will also occur, resulting in a wide spectrum of internal waves (Hibiya *et al.*, 2002). Sediment waves generated by internal waves at a deeper location on the Israeli shelf exhibit wavelengths in the range of 10 s to 100 s of metres (Reiche

et al., 2018), while the bedforms observed at Bustan HaGalil Ridge are at the metre scale. Internal waves have been imaged with multi-channel seismic west of the study area in the same depth range as the observed bedforms (Fig. 13). Visualisation of internal waves using satellite data is difficult in this region due to local interferences, but their presence can be inferred from them (Appendix S1, Fig. S1.7). Based on the multi-channel seismic section, the internal waves exhibit wavelengths in the range of 10 s of metres and a metre-scale amplitude. Large-scale sediment waves (10 s to 100 s of metres) are attributed to internal waves with wavelengths of hundreds of metres (Reiche *et al.*, 2018), which have a wide range of frequencies in the region (Solodoch *et al.*, 2023), whereas the metre-scale dunes described here likely result from pycnocline internal waves with wavelengths of tens of metres. In both cases, the wavelengths of the sediment waves/dunes are one or two orders lower than the wavelengths from the imaged internal waves. As along-slope currents and surface waves alone are unlikely to explain the observed bedforms and internal waves occur within the study area, internal waves are suggested as the most likely cause for the dunes.

The zigzag-like or v-shaped pattern of the chevron bedforms and their location within the valleys (with preference on the northern side, Fig. 11A) suggests a complex formation mechanism that varies spatially and/or temporally. The chevron bedforms also occur superimposed on the dunes (mixed bedforms). The so-called tile-shaped interference ripples and ladderback ripples (Dumas *et al.*, 2005; Baas *et al.*, 2021) have a similar morphology as the chevron bedforms and mixed bedforms documented here. However, the difference between the cases is that the shallower bedforms occur on a cm-scale instead of the metres-scale bedforms found in the study area. These bedforms in shallower environments have been attributed to interference patterns between surface waves and currents (Dumas *et al.*, 2005; Baas *et al.*, 2021). Following this mechanism, interference between bottom currents and internal waves is suggested to generate the chevron and mixed bedforms.

It appears that the chevron bedforms are present where the sediment layer is thinner, while dunes correspond to a thicker layer of sediment in the valleys. Based on the SBP data, the maximum thickness of the sediment in the valleys is ~0.5 m. Divers in the area have reported the bedforms to have a relief in the decimetre scale (personal communication). Possibly, a thin layer of sediment provides not enough material for the dunes to grow as high as in areas with a thicker sediment layer, which makes them less stable. Dunes that have more sediment to grow might destroy the smaller structures formed by along-slope bottom current. This remains speculative because of the uncertainty of the sediment thickness and the bedform relief. In a current-controlled setting, there may also be a correlation between sediment grain size and sediment thickness. However, if such a correlation exists, it could mean that the formation of the bedforms depends on sediment grain size and not sediment thickness. At the moment, this hypothesis cannot be evaluated due to the lack of well-distributed sediment samples in the area. Incorporating additional sediment samples, physical modelling or numerical simulations will advance our understanding of bedform dynamics in the future.

The ultra-high resolution of the SAS facilitates the identification of the bedforms, as bathymetric data alone cannot clearly resolve these features. Likely, features of similar magnitude forming elsewhere have been missed due to limitations of the imaging technology. The findings from Bustan HaGalil Ridge support the argument that internal waves play an important role in modulating turbidity and sediment distribution in mesophotic settings (Pomar *et al.*, 2012). However, they are not the only mechanism at play in this environment. The asymmetry of the ridges, the occurrence of chevron bedforms and the moat-drift contourite systems indicate that regional bottom currents are also responsible for shaping the seafloor. Moreover, while coralline algae nodules require only slight agitation (Marrack, 1999), the distribution of the sediment grain sizes (Fig. 11D and E) suggests the influence of significant transport energy. The existence of the mixed bedforms also indicates that the shaping mechanisms vary spatially. This interaction between regional bottom currents and internal waves most likely contributes also to shaping the coralligenous build-ups. The mechanisms observed here are likely to also be present in open ocean mesophotic systems. In the Mascarene Plateau, for example, bottom currents and internal waves have been shown to be important factors for seafloor remodelling in mesophotic to shallow aphotic depths (Betzler *et al.*, 2023; Bialik *et al.*, 2024). However, while internal waves (Davis & Monismith, 2011;

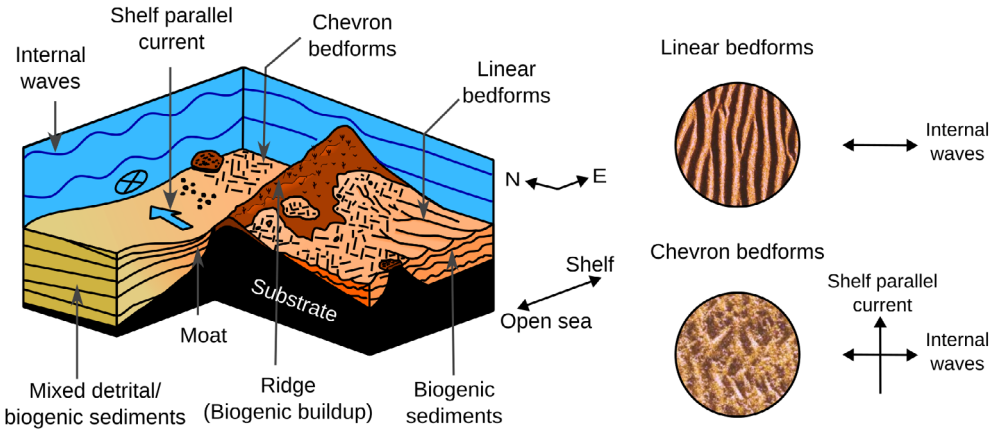

Fig. 15. Schematic model (not to scale) of the bedform configuration and processes at play in the Bustan HaGalil Ridge.

Wall *et al.*, 2012; Johnston & Colin, 2022; Marmorino, 2024) and bottom currents (Correa *et al.*, 2012; Locker *et al.*, 2016) have both been reported to interact with deeper reefs, there are few reports of both occurring at the same time. This is possibly due to the different techniques usually used to detect them. To further understand the observed interference patterns and especially the temporal variability of the bedforms, repeated measurements in the same area are needed, together with mooring stations to measure internal waves and current velocity near the seafloor.

CONCLUSIONS

Mesophotic reefs represent crucial environments for maintaining high biodiversity as they might be important as a refugia for species affected by environmental stress (Bongaerts *et al.*, 2010; Martinez *et al.*, 2021). However, they are still an underexplored marine niche. Sediment distribution in these settings is only poorly understood. In this study, high-resolution acoustic imaging of a mesophotic reef in the south-eastern Mediterranean Sea was carried out. With cutting-edge imaging, it is possible to observe a mosaic of hard substrate reefs and maerl (rhodolith) beds interspersed with locally produced, coarse-grained, biogenic sediment that forms two types of metre-scale bedforms. Part of the sediment is transported northward as bedload by the bottom current, where it is blocked by the ridges/reef, leading to an asymmetry of the slopes (Fig. 15). Furthermore, northward flowing bottom currents lead to a constructional moat-drift system on the western side of the reef, highlighting the importance of bottom currents in shaping the reef. The large linear bedforms with a S–N orientation (here classified as dunes) are likely created by internal waves. The chevron bedforms are likely interference patterns created by the interaction between along-slope currents and internal waves (Fig. 15). Similar bedforms might also occur in other mesophotic reefs but have previously not been studied in detail because of the absence of ultra-high resolution hydroacoustic imaging. Future studies incorporating high-resolution imaging with large spatial coverage (acoustic and/or photogrammetry), well-distributed sediment sampling, repeated measurements, physical modelling and numerical simulations will advance our understanding of bedform dynamics in and around mesophotic reefs.

ACKNOWLEDGEMENTS

OMB and HW are acknowledged as equal contributors. The data acquisition and initial analysis for this study were funded by the Israel Nature and Parks Authority and the Israel Society of Ecology and Environmental Sciences in the framework of the Science for MPA project. Funding was also provided by the Leon H. Charney School of Marine Sciences (CSMS), University of Haifa and Kadas family (Kadas Nexus, Morris Kahn Marine Research Station, CSMS). Part of this study was conducted as part of

OMB's Marie Skłodowska Curie fellowship (101003394—RhodoMalta). OMB and HW were partially supported by the German (GEOMAR)—Israeli (University of Haifa) Helmholtz International Laboratory: The Eastern Mediterranean Sea Centre—An Early-Warning Model-System for our Future Oceans (EMS FORE). OG was supported by Marie Skłodowska Curie Fellowship—101180613—GEM-SBP. AM was supported by the David and Lucile Packard Foundation. We thank Emerson-Aspentech for contributing their SSE software suite; the AUV survey teams of the University of Haifa Subsea Vehicles facility and S/V Shiqmona for collecting the geophysical data; and the technical diving teams of the Morris Kahn Marine Research Station and the Putsker Diving Center for the samples and visual data collection. The oceanographic buoy observatory data were kindly shared by the Texas A&M—University of Haifa—Eastern Mediterranean Observatory (THEMO) project. THEMO is operated by the Underwater Acoustic and Navigation Laboratory (ANL), Hatter Department of Marine Technology, University of Haifa, Israel, and by the Geochemical and Environmental Research Group (GERG), Texas A&M University, USA, and co-funded by the respective universities.

DATA AVAILABILITY STATEMENT

All supplementary and ancillary datasets are available via Figshare at https://figshare.com/s/6165f5654b4fb00183e7 with doi: 10.6084/m9.figshare.19642449. This study has been conducted using E.U. Copernicus Marine Service Information (https://doi.org/10.48670/moi-00016).

REFERENCES

Albano, P.G., **Azzarone, M.**, **Amati, B.**, **Bogi, C.**, **Sabelli, B.** and **Rilov, G.** (2020) Low diversity or poorly explored? Mesophotic molluscs highlight undersampling in the Eastern Mediterranean. *Biodivers. Conserv.*, **29**, 4059–4072.

Alford, M.H., **MacKinnon, J.A.**, **Simmons, H.L.** and **Nash, J.D.** (2016) Near-inertial internal gravity waves in the ocean. *Annu. Rev. Mar. Sci.*, **8**, 95–123.

Alhammoud, B., **Béranger, K.**, **Mortier, L.**, **Crépon, M.** and **Dekeyser, I.** (2005) Surface circulation of the Levantine Basin: comparison of model results with observations. *Prog. Oceanogr.*, **66**, 299–320.

Allen, J.R.L. (1985) *Principles of Physical Sedimentology*, p. 272. Chapman and Hall, London.

Almagor, G., **Gill, D.** and **Perath, I.** (2000) Marine sand resources offshore Israel. *Mar. Georesour. Geotechnol.*, **18**, 1–42.

Almogi-Labin, A., **Calvo, R.**, **Elyashiv, H.**, **Amit, R.**, **Harlavan, Y.** and **Herut, B.** (2012) Sediment Characterization of the Israeli Mediterranean Shelf (10–100 m), p. 42. Jerusalem. Geology Survey of Israel report GSI/27/2012.

Alwany, M.A., **Thaler, E.** and **Stachowitsch, M.** (2009) Parrotfish bioerosion on Egyptian Red Sea reefs. *J. Exp. Mar. Biol. Ecol.*, **371**, 170–176.

Amado-Filho, G.M., **Moura, R.L.**, **Bastos, A.C.**, **Francini-Filho, R.B.**, **Pereira-Filho, G.H.**, **Bahia, R.G.**, **Moraes, F.C.** and **Motta, F.S.** (2016) Mesophotic ecosystems of the unique South Atlantic atoll are composed by rhodolith beds and scattered consolidated reefs. *Mar. Biodivers.*, **46**, 933–936.

Ashley, G.M. (1990) Classification of large-scale subaqueous bedforms; a new look at an old problem. *J. Sed. Res.*, **60**, 160–172.

Baas, J.H., **Malarkey, J.**, **Lichtman, I.D.**, **Amoudry, L.O.**, **Thorne, P.D.**, **Hope, J.A.**, **Peakall, J.**, **Paterson, D.M.**, **Bass, S.J.**, **Cooke, R.D.**, **Manning, A.J.**, **Parsons, D.R.** and **Ye, L.** (2021) Current- and wave-generated bedforms on mixed sand–clay intertidal flats: a new bedform phase diagram and implications for bed roughness and preservation potential. *Front. Earth Sci.*, **9**, 747567.

Baker, E.K., **Puglise, K.A.**, **Colin, P.**, **Harris, P.T.**, **Kahng, S.E.**, **Rooney, J.J.**, **Sherman, C.**, **Slattery, M.** and **Spalding, H.** (2016) What are mesophotic coral ecosystems? In: *Mesophotic Coral Ecosystems—A Lifeboat for Coral Reefs?* (Eds Baker, E.K., Puglise, K.A. and Harris, P.T.), pp. 11–19. The United Nations Environment Programme and GRID-Arendal, Nairobi.

Ballesteros, E., **Avançats, E.** and **Csic, D.B.** (2006) Mediterranean coralligenous assemblages: a synthesis of present knowledge. *Oceanogr. Mar. Biol. Annu. Rev.*, **44**, 123–195.

Bell, J.J., **Micaroni, V.**, **Harris, B.**, **Strano, F.**, **Broadribb, M.** and **Rogers, A.** (2024) Global status, impacts, and management of rocky temperate mesophotic ecosystems. *Conserv. Biol.*, **38**, e13945.

Berman, T., **Azov, Y.** and **Townsend, D.** (1984) Understanding oligotrophic oceans: can the eastern Mediterranean be a useful model? In: *Marine Phytoplankton and Productivity* (Eds Holm-Hansen, O., Bolis, L. and Gilles, R.), *Lecture Notes on Coastal and Estuarine Studies*, **8**. Springer, Berlin, Heidelberg.

Betzler, C., **Lindhorst, S.**, **Reijmer, J.J.G.**, **Braga, J.C.**, **Lüdmann, T.**, **Bialik, O.M.**, **Reolid, J.**, **Geßner, A.**, **Hainbucher, D.** and **Bissessur, D.** (2023) Carbonate platform drowning caught in the act: the sedimentology of Saya de Malha Bank (Indian Ocean). *Sedimentology*, **70**, 78–99.

Bialik, O.M., **Betzler, C.**, **Braga, J.C.**, **Reijmer, J.J.G.**, **Reolid, J.** and **Lindhorst, S.** (2024) Changes in mesophotic carbonate-platform export across the end of the last glacial cycle (Saya de Malha Bank, western Indian Ocean). *Depos. Rec.*, **10**, 374–397.

Bialik, O.M., **Varzi, A.G.**, **Durán, R.**, **Le Bas, T.**, **Gauci, A.**, **Savini, A.** and **Micallef, A.** (2022) Mesophotic depth biogenic accumulations ("biogenic mounds") offshore the Maltese Islands, Central Mediterranean Sea. *Front. Mar. Sci.*, **9**, 803687.

Bianchi, C.N. and **Morri, C.** (2003) Global sea warming and "tropicalization" of the Mediterranean Sea: biogeographic and ecological aspects. *Biogeogr. J. Integr. Biogeogr.*, **24**, 319–327.

Boegman, L. and **Ivey, G.N.** (2009) Flow separation and resuspension beneath shoaling nonlinear internal waves. *J. Geophys. Res. Oceans*, **114**, 1–15.

Boegman, L. and **Stastna, M.** (2019) Sediment resuspension and transport by internal solitary waves. *Annu. Rev. Fluid Mech.*, **51**, 129–154.

Bongaerts, P., **Frade, P.R.**, **Ogier, J.J.**, **Hay, K.B.**, **van Bleijswijk, J.**, **Englebert, N.**, **Vermeij, M.J.**, **Bak, R.P.**, **Visser, P.M.** and **Hoegh-Guldberg, O.** (2013) Sharing the slope: depth partitioning of agariciid corals and associated Symbiodinium across shallow and mesophotic habitats (2–60 m) on a Caribbean reef. *BMC Evol. Biol.*, **13**, 205.

Bongaerts, P., **Ridgway, T.**, **Sampayo, E.M.** and **Hoegh-Guldberg, O.** (2010) Assessing the 'deep reef refugia' hypothesis: focus on Caribbean reefs. *Coral Reefs*, **29**, 309–327.

Bradford, J.M. and **Chang, F.H.** (1987) Standing stocks and productivity of phytoplankton off Westland, New Zealand, February 1982. *NZ J. Mar. Freshwat. Res.*, **21**, 71–90.

Braga, J.C. and **Martín, J.** (1988) Neogene coralline-algal growth-forms and their palaeoenvironments in the Almanzora river valley (Almeria, S.E. Spain). *Palaeogeogr. Palaeoclimatol. Palaeoecol.*, **67**, 285–303.

Braithwaite, C.J.R., **Taylor, J.D.** and **Glover, E.A.** (2000) Marine carbonate cements, biofilms, biomineralization, and skeletogeneis: some bivalves do it all. *J. Sed. Res.*, **70**, 1129–1138.

Brokovich, E., **Einbinder, S.**, **Shashar, N.**, **Kiflawi, M.** and **Kark, S.** (2008) Descending to the twilight-zone: changes in coral reef fish assemblages along a depth gradient down to 65 m. *Mar. Ecol. Prog. Ser.*, **371**, 253–262.

Cacchione, D.A. (1970) *Experimental Study of Internal Gravity Waves Over a Slope*. Massachusetts Institute of Technology and Woods Hole Oceanographic Institution, Woods Hole, MA.

Cacchione, D.A. and **Drake, D.E.** (1986) Nepheloid layers and internal waves over continental shelves and slopes. *Geo-Mar. Lett.*, **6**, 147–152.

Cerrano, C., **Bastari, A.**, **Calcinai, B.**, **Di Camillo, C.**, **Pica, D.**, **Puce, S.**, **Valisano, L.** and **Torsani, F.** (2019) Temperate mesophotic ecosystems: gaps and perspectives of an emerging conservation challenge for the Mediterranean Sea. *Eur. Zool. J.*, **86**, 370–388.

Cerrano, C., **Danovaro, R.**, **Gambi, C.**, **Pusceddu, A.**, **Riva, A.** and **Schiaparelli, S.** (2010) Gold coral (*Savalia savaglia*) and gorgonian forests enhance benthic biodiversity and ecosystem functioning in the mesophotic zone. *Biodivers. Conserv.*, **19**, 153–167.

Cheriton, O.M., **McPhee-Shaw, E.E.**, **Shaw, W.J.**, **Stanton, T.P.**, **Bellingham, J.G.** and **Storlazzi, C.D.** (2014) Suspended particulate layers and internal waves over the southern Monterey Bay continental shelf: an important control on shelf mud belts? *J. Geophys. Res. Oceans*, **119**, 428–444.

Church, J.A., **Andrews, J.C.** and **Boland, F.M.** (1985) Tidal currents in the central Great Barrier Reef. *Cont. Shelf Res.*, **4**, 515–531.

Clifton, H.E. and **Dingler, J.R.** (1984) Wave-formed structures and paleoenvironmental reconstruction. *Mar. Geol.*, **60**, 165–198.

Correa, T.B.S., **Eberli, G.P.**, **Grasmueck, M.**, **Reed, J.K.** and **Correa, A.M.S.** (2012) Genesis and morphology of cold-water coral ridges in a unidirectional current regime. *Mar. Geol.*, **326–328**, 14–27.

Corriero, G., **Pierri, C.**, **Mercurio, M.**, **Nonnis Marzano, C.**, **Onen Tarantini, S.**, **Gravina, M.F.**, **Lisco, S.**, **Moretti, M.**, **De Giosa, F.**, **Valenzano, E.**, **Giangrande, A.**, **Mastrodonato, M.**, **Longo, C.** and **Cardone, F.** (2019) A Mediterranean mesophotic coral reef built by non-symbiotic scleractinians. *Sci. Rep.*, **9**, 3601.

Davis, K.A. and **Monismith, S.G.** (2011) The modification of bottom boundary layer turbulence and mixing by internal waves shoaling on a barrier reef. *J. Phys. Oceanogr.*, **41**, 2223–2241.

Dimitrijević, D., **Santodomingo, N.** and **Kiessling, W.** (2024) Reef refugia in the aftermath of past episodes of global warming. *Coral Reefs*, **43**, 1431–1442.

Droghei, R., **Falcini, F.**, **Casalbore, D.**, **Martorelli, E.**, **Mosetti, R.**, **Sannino, G.**, **Santoleri, R.** and **Chiocci, F.L.** (2016) The role of internal solitary waves on deep-water sedimentary processes: the case of up-slope migrating sediment waves off the Messina Strait. *Sci. Rep.*, **6**, 36376.

Dulin, T., **Avnaim-Katav, S.**, **Sisma-Ventura, G.**, **Bialik, O.M.** and **Angel, D.L.** (2020) Rhodolith beds along the southeastern Mediterranean inner shelf: implications for past depositional environments. *J. Mar. Syst.*, **201**, 103241.

Dumas, S., **Arnott, R.W.C.** and **Southard, J.B.** (2005) Experiments on oscillatory-flow and combined-flow bed forms: implications for interpreting parts of the shallow-marine sedimentary record. *J. Sed. Res.*, **75**, 501–513.

Edelist, D., **Rilov, G.**, **Golani, D.**, **Carlton, J.T.** and **Spanier, E.** (2013) Restructuring the sea: profound shifts in the world's most invaded marine ecosystem. *Divers. Distrib.*, **19**, 69–77.

Emery, K.O. and **Bentor, Y.K.** (1960) *The Continental Shelf of Israel*, pp. 25–41. Ministry of Development, Geological Survey, State of Israel.

Eyal, G., **Laverick, J.H.**, **Bongaerts, P.**, **Levy, O.** and **Pandolfi, J.M.** (2021) Mesophotic coral ecosystems of the Great Barrier Reef are understudied and underexplored. *Front. Mar. Sci.*, **8**, 622856.

Eytam, Y. and **Ben-Avraham, Z.** (1992) Morphology and sediments of the inner shelf off northern Israel. *Isr. J. Earth Sci.*, **41**, 27–44.

Faugères, J.-C. and **Mulder, T.** (2011) Contour currents and contourite drifts. In: *Deep-Sea Sediments, Developments in Sedimentology 63* (Eds Huneke, H. and Mulder, T.), pp. 149–214. Elsevier, Amsterdam.

Faugères, J.-C., **Stow, D.A.V.**, **Imbert, P.** and **Viana, A.** (1999) Seismic features diagnostic of contourite drifts. *Mar. Geol.*, **162**, 1–38.

Flemming, B.W. (2024) The concept of wave base: fact and fiction. *Geo-Mar. Lett.*, **44**, 14.

García-Charton, J.A. and **Pérez-Ruzafa, Á.** (2001) Spatial pattern and the habitat structure of a Mediterranean rocky reef fish local assemblage. *Mar. Biol.*, **138**, 917–934.

Garrett, C. and **Munk, W.** (1979) Internal waves in the ocean. *Annu. Rev. Fluid Mech.*, **11**, 339–369.

Golik, A. (1993) Indirect evidence for sediment transport on the continental shelf off Israel. *Geo-Mar. Lett.*, **13**, 159–164.

Goren, L., **Idan, T.**, **Shefer, S.** and **Ilan, M.** (2021) Macrofauna inhabiting massive demosponges from shallow and mesophotic habitats along the Israeli Mediterranean coast. *Front. Mar. Sci.*, **7**, 612779.

Grabau, A.W. (1904) *On the Classification of Sedimentary Rocks*, p. 247. Wentworth Press, New York, NY.

Grossowicz, M., **Bialik, O.M.**, **Shemesh, E.**, **Tchernov, D.**, **Vonhof, H.B.** and **Sisma-Ventura, G.** (2020) Ocean warming is the key filter for successful colonization of the migrant octocoral *Melithaea erythraea* (Ehrenberg, 1834) in the Eastern Mediterranean Sea. *PeerJ*, **8**, e9355.

Helfrich, K.R. and **Melville, W.K.** (2006) Long nonlinear internal waves. *Annu. Rev. Fluid Mech.*, **38**, 395–425.

Hernández, R., **Sherman, C.**, **Weil, E.** and **Yoshioka, P.** (2009) Spatial and temporal patterns in reef sediment accumulation and composition, southwestern insular shelf of Puerto Rico. *Caribb. J. Sci.*, **45**, 138–150.

Hibiya, T., **Nagasawa, M.** and **Niwa, Y.** (2002) Nonlinear energy transfer within the oceanic internal wave spectrum at mid and high latitudes. *J. Geophys. Res. Oceans*, **107**, 28-1–28-8.

Hopfauf, V., **Spiess, V.** and **Geowissenschaften, F.** (2001) A three-dimensional theory for the development and migration of deep sea sedimentary waves. *Deep Sea Res. Part I Oceanogr. Res. Pap.*, **48**, 2497–2519.

Hottinger, L. (1983) Neritic macroid genesis, an ecological approach. In: *Coated Grains* (Ed Peryt, T.M.), pp. 38–55. Springer Berlin Heidelberg, Berlin, Heidelberg.

Idan, T., **Shefer, S.**, **Feldstein, T.**, **Yahel, R.**, **Huchon, D.** and **Ilan, M.** (2018) Shedding light on an East-Mediterranean mesophotic sponge ground community and the regional sponge fauna. *Mediterr. Mar. Sci.*, **19**, 84.

Ingrosso, G., **Abbiati, M.**, **Badalamenti, F.**, **Bavestrello, G.**, **Belmonte, G.**, **Cannas, R.**, **Benedetti-Cecchi, L.**, **Bertolino, M.**, **Bevilacqua, S.**, **Bianchi, C.N.**, **Bo, M.**, **Boscari, E.**, **Cardone, F.**, **Cattaneo-Vietti, R.**, **Cau, A.**, **Cerrano, C.**, **Chemello, R.**, **Chimienti, G.**, **Congiu, L.**, **Corriero, G.**, **Costantini, F.**, **De Leo, F.**, **Donnarumma, L.**, **Falace, A.**, **Fraschetti, S.**, **Giangrande, A.**, **Gravina, M.F.**, **Guarnieri, G.**, **Mastrototaro, F.**, **Milazzo, M.**, **Morri, C.**, **Musco, L.**, **Pezzolesi, L.**, **Piraino, S.**, **Prada, F.**, **Ponti, M.**, **Rindi, F.**, **Russo, G.F.**, **Sandulli, R.**, **Villamor, A.**, **Zane, L.** and **Boero, F.** (2018) Mediterranean bioconstructions along the Italian coast. *Adv. Mar. Biol.*, **78**, 61–136.

James, N.P. and **Lukasik, J.J.** (2010) Cool- and cold-water neritic carbonates. In: *Facies Models 4* (Eds James, N.P. and Dalymple, R.W.), pp. 371–399. Geolocial Association of Canada, St. John.

James, N.P., **Collins, L.B.**, **Bone, Y.** and **Hallock, P.** (1999) Subtropical carbonates in a temperate realm; modern sediments on the Southwest Australian shelf. *J. Sed. Res.*, **69**, 1297–1321.

Johnston, T.M.S. and **Colin, P.L.** (2022) Upwelling and downwelling driven by the north equatorial countercurrent and internal waves at Hatohobei Island and Helen Reef, Palau. *J. Geophys. Res. Oceans*, **127**, e2021JC017606.

Kahng, S.E., **Akkaynak, D.**, **Shlesinger, T.**, **Hochberg, E.J.**, **Wiedenmann, J.**, **Tamir, R.** and **Tchernov, D.** (2019) Light, temperature, photosynthesis, heterotrophy, and the lower depth limits of mesophotic coral ecosystems. In: *Mesophotic Coral Ecosystems* (Eds Loya, Y., Puglise, K. and Bridge, T.), *Coral Reefs of the World*, **12**, 801–828. Springer, Cham.

Kahng, S.E., **Copus, J.** and **Wagner, D.** (2014) Recent advances in the ecology of mesophotic coral ecosystems (MCEs). *Curr. Opin. Environ. Sustain.*, **7**, 72–81.

Kahng, S.E., **Garcia-Sais, J.R.**, **Spalding, H.L.**, **Brokovich, E.**, **Wagner, D.**, **Weil, E.**, **Hinderstein, L.** and **Toonen, R.J.** (2010) Community ecology of mesophotic coral reef ecosystems. *Coral Reefs*, **29**, 255–275.

Kahru, M. (1983) Phytoplankton patchiness generated by long internal waves: a model. *Mar. Ecol. Prog. Ser.*, **10**, 111–117.

Katz, T. and **Crouvi, O.** (2018) Sediment flux dynamics over the shallow (25 m depth) shelf of the Mediterranean Sea along the Israeli coast. *Mar. Geol.*, **406**, 1–11.

Katz, T., **Yahel, G.**, **Reidenbach, M.**, **Tunnicliffe, V.**, **Herut, B.**, **Crusius, J.**, **Whitney, F.**, **Snelgrove, P.V.R.** and **Lazar, B.** (2012) Resuspension by fish facilitates the transport and redistribution of coastal sediments. *Limnol. Oceanogr.*, **57**, 945–958.

Kolla, V., **Eittreim, S.**, **Sullivan, L.**, **Kostecki, J.A.** and **Burckle, L.H.** (1980) Current-controlled, abyssal microtopography and sedimentation in Mozambique Basin, southwest Indian Ocean. *Mar. Geol.*, **34**, 171–206.

Kress, N. and **Herut, B.** (2001) Spatial and seasonal evolution of dissolved oxygen and nutrients in the Southern Levantine Basin (Eastern Mediterranean Sea): chemical characterization of the water masses and inferences on the N:P ratios. *Deep Sea Res. Part I Oceanogr. Res. Pap.*, **48**, 2347–2372.

Krom, M.D., **Woodward, E.M.S.**, **Herut, B.**, **Kress, N.**, **Carbo, P.**, **Mantoura, R.F.C.**, **Spyres, G.**, **Thingstad, T.F.**, **Wassmann, P.**, **Wexels-Riser, C.**, **Kitidis, V.**, **Law, C.S.** and **Zodiatis, G.** (2005) Nutrient cycling in the south east Levantine basin of the eastern Mediterranean: results from a phosphorus starved system. *Deep Sea Res. Part II Top. Stud. Oceanogr.*, **52**, 2879–2896.

Lamb, K.G. (2014) Internal wave breaking and dissipation mechanisms on the continental slope/shelf. *Annu. Rev. Fluid Mech.*, **46**, 231–254.

Laverick, J.H., **Tamir, R.**, **Eyal, G.** and **Loya, Y.** (2020) A generalized light-driven model of community transitions along coral reef depth gradients. *Glob. Ecol. Biogeogr.*, **29**, 1554–1564.

Leichter, J.J., **Shellenbarger, G.** and **Genovese, S.J.** (1998) Breaking internal waves on a Florida (USA) coral reef: a plankton pump at work? *Mar. Ecol. Prog. Ser.*, **166**, 83–97.

Lesser, M.P., **Slattery, M.** and **Leichter, J.J.** (2009) Ecology of mesophotic coral reefs. *J. Exp. Mar. Biol. Ecol.*, **375**, 1–8.

Lesser, M.P., **Slattery, M.** and **Mobley, C.D.** (2018) Biodiversity and functional ecology of mesophotic coral reefs. *Annu. Rev. Ecol. Evol. Syst.*, **49**, 49–71.

Li, G., **Cheng, L.**, **Zhu, J.**, **Trenberth, K.E.**, **Mann, M.E.** and **Abraham, J.P.** (2020) Increasing ocean stratification over the past half-century. *Nat. Clim. Chang.*, **10**, 1116–1123.

Locker, S.D., **Reed, J.K.**, **Farrington, S.**, **Harter, S.**, **Hine, A.C.** and **Dunn, S.** (2016) Geology and biology of the "Sticky Grounds", shelf-margin carbonate mounds, and mesophotic ecosystem in the eastern Gulf of Mexico. *Cont. Shelf Res.*, **125**, 71–87.

Marmorino, G. (2024) A first look at internal waves in the great barrier reef lagoon. *Remote Sens.*, **16**, 2180.

Marrack, E.C. (1999) The relationship between water motion and living Rhodolith beds in the Southwestern Gulf of California, Mexico. *Palaios*, **14**, 159.

Martinez, S., **Bellworthy, J.**, **Ferrier-Pagès, C.** and **Mass, T.** (2021) Selection of mesophotic habitats by *Oculina patagonica* in the Eastern Mediterranean Sea following global warming. *Sci. Rep.*, **11**, 18134.

Mauz, B., **Hijma, M.P.**, **Amorosi, a.**, **Porat, N.**, **Galili, E.** and **Bloemendal, J.** (2013) Aeolian beach ridges and their significance for climate and sea level: concept and insight from the Levant coast (East Mediterranean). *Earth Sci. Rev.*, **121**, 31–54.

Megard, R.O. and **Berman, T.** (1989) Effects of algae on the Secchi transparency of the southeastern Mediterranean Sea. *Limnol. Oceanogr.*, **34**, 1640–1655.

Menza, C., **Kendall, M.** and **Hile, S.** (2007) The deeper we go the less we know. *Rev. Biol. Trop.*, **56**, 11–24.

Miramontes, E., **Jouet, G.**, **Thereau, E.**, **Bruno, M.**, **Penven, P.**, **Guerin, C.**, **Le Roy, P.**, **Droz, L.**, **Jorry, S.J.**, **Hernández-Molina, F.J.**, **Thiéblemont, A.**, **Silva Jacinto, R.** and **Cattaneo, A.** (2020) The impact of internal waves on upper continental slopes: insights from the Mozambican margin (southwest Indian Ocean). *Earth Surf. Proc. Landf.*, **45**, 1469–1482.

Miramontes, E., **Thiéblemont, A.**, **Babonneau, N.**, **Penven, P.**, **Raisson, F.**, **Droz, L.**, **Jorry, S.J.**, **Fierens, R.**, **Counts, J.W.**, **Wilckens, H.**, **Cattaneo, A.** and **Jouet, G.** (2021) Contourite and mixed turbidite-contourite systems in the Mozambique Channel (SW Indian Ocean): link between geometry, sediment characteristics and modelled bottom currents. *Mar. Geol.*, **437**, 106502.

Mitchell, B.G., **Bricaud, A.**, **Carder, K.**, **Cleveland, J.**, **Ferrari, G.**, **Gould, R.**, **Kahru, M.**, **Kishino, M.**, **Maske, H.**, **Moisan, T.**, **Moore, L.**, **Nelson, N.**, **Phinney, D.**, **Reynolds, R.**, **Sosik, H.**, **Stramski, D.**, **Tassan, S.**, **Trees, C.**, **Weidemann, A.** and **Vodacek, A.** (2000) Determination of spectral absorption coefficients of particles, dissolved material and phytoplankton for discrete water samples. *NASA Tech. Memo.*, **4**, 125–153.

Morsilli, M. and **Pomar, L.** (2012) Internal waves vs. surface storm waves: a review on the origin of hummocky cross-stratification. *Terra Nova*, **24**, 273–282.

Munk, W. (1981) Internal waves and small-scale processes. In: *Evolution of Physical Oceanography* (Eds Warren, B.A. and Wunsch, C.), pp. 264–291. MIT Press, Cambridge, MT.

Nagasawa, M., **Niwa, Y.** and **Hibiya, T.** (2000) Spatial and temporal distribution of the wind-induced internal wave energy available for deep water mixing in the North Pacific. *J. Geophys. Res. Oceans*, **105**, 13933–13943.

Nanson, R., **Arosio, R.**, **Gafeira, J.**, **McNeil, M.**, **Dove, D.**, **Bjarnadóttir, L.R.**, **Dolan, M.F.J.**, **Guinan, J.**, **Post, A.**, **Webb, J.** and **Nichol, S.** (2023) *A Two-Part Seabed Geomorphology Classification Scheme*, p. 95. EGU General Assembly, Vienna, Austria.

Neev, D., **Bakler, N.** and **Emery, K.O.** (1987) *Mediterranean Coasts of Israel and Sinai: Holocene Tectonism from Geology, Geophysics, and Archaelogy*, p. 148. Taylor & Francis, New York.

Nielsen, S.G., **Mar-Gerrison, S.**, **Gannoun, A.**, **LaRowe, D.**, **Klemm, V.**, **Halliday, A.N.**, **Burton, K.W.** and **Hein, J.R.** (2009) Thallium isotope evidence for a permanent increase in marine organic carbon export in the early Eocene. *Earth Planet. Sci. Lett.*, **278**, 297–307.

Ofir, E., **Corrales, X.**, **Coll, M.**, **Heymans, J.J.**, **Goren, M.**, **Steenbeek, J.**, **Amitai, Y.**, **Shachar, N.** and **Gal, G.** (2023) Evaluation of fisheries management policies in the alien species-rich Eastern Mediterranean under climate change. *Front. Mar. Sci.*, **10**. https://doi.org/10.3389/fmars.2023.1155480.

Ozer, T., **Gertman, I.**, **Kress, N.**, **Silverman, J.** and **Herut, B.** (2017) Interannual thermohaline (1979–2014) and nutrient (2002–2014) dynamics in the Levantine surface and intermediate water masses, SE Mediterranean Sea. *Glob. Planet. Chang.*, **151**, 60–67.

Paulat, M., **Lüdmann, T.**, **Betzler, C.** and **Eberli, G.P.** (2019) Neogene palaeoceanographic changes recorded in a carbonate contourite drift (Santaren Channel, Bahamas). *Sedimentology*, **66**, 1361–1385.

Peleg, O., **Guy-Haim, T.**, **Yeruham, E.**, **Silverman, J.** and **Rilov, G.** (2020) Tropicalization may invert trophic state and carbon budget of shallow temperate rocky reefs. *J. Ecol.*, **108**, 844–854.

Pelinovksy, E., **Talipova, T.** and **Ivanov, V.** (1995) Estimations of the nonlinear properties of the internal wave field off the Israel coast. *Nonlinear Process. Geophys.*, **2**, 80–88.

Polton, J.A., **Smith, J.A.**, **MacKinnon, J.A.** and **Tejada-Martínez, A.E.** (2008) Rapid generation of high-frequency internal waves beneath a wind and wave forced oceanic surface mixed layer. *Geophys. Res. Lett.*, **35**, L13602.

Pomar, L., **Baceta, J.I.**, **Hallock, P.**, **Mateu-Vicens, G.** and **Basso, D.** (2017) Reef building and carbonate production modes in the west-central Tethys during the Cenozoic. *Mar. Pet. Geol.*, **83**, 261–304.

Pomar, L., **Morsilli, M.**, **Hallock, P.** and **Bádenas, B.** (2012) Internal waves, an under-explored source of turbulence events in the sedimentary record. *Earth Sci. Rev.*, **111**, 56–81.

Porat, N., **Wintle, A.G.** and **Ritte, M.** (2003) Mode and timing of kurkar and hamra formation, central coastal plain, Israel. *Isr. J. Earth Sci.*, **53**, 13–25.

Quaresma, L.S., **Vitorino, J.**, **Oliveira, A.** and **da Silva, J.** (2007) Evidence of sediment resuspension by nonlinear internal waves on the western Portuguese mid-shelf. *Mar. Geol.*, **246**, 123–143.

R Core Team (2024) *R: a Language and Environment for Statistical Computing*. R Foundation for Statistical Computing, Vienna, Austria. http://www.r-project.org/.

Reich, T., **Ben-Ezra, T.**, **Belkin, N.**, **Tsemel, A.**, **Aharonovich, D.**, **Roth-Rosenberg, D.**, **Givati, S.**, **Bialik, O.**, **Herut, B.**, **Berman-Frank, I.**, **Frada, M.**, **Krom, M.D.**, **Lehahn, Y.**, **Rahav, E.** and **Sher, D.** (2021) Seasonal dynamics of phytoplankton and bacterioplankton at the ultra-oligotrophic southeastern Mediterranean Sea. *bioRxiv*. https://doi.org/10.1101/2021.03.24.436734.

Reiche, S., **Hübscher, C.**, **Brenner, S.**, **Betzler, C.** and **Hall, J.K.** (2018) The role of internal waves in the late quaternary evolution of the Israeli continental slope. *Mar. Geol.*, **406**, 177–192.

Ribó, M., **Puig, P.**, **Muñóz, A.**, **Iacono, C.L.**, **Masqué, P.**, **Palanques, A.**, **Acosta, J.**, **Guillén, J.** and **Ballesteros, M.G.** (2017) Large-scale fine-grained sediment waves over the Gulf of Valencia Continental Slope (NW Mediterranean). In: *Atlas of Bedforms in the Western Mediterranean* (Eds Guillén, J., Acosta, J., Chiocci, F. and Palanques, A.), pp. 265–271. Springer International Publishing, Cham.

Richardson, K. and **Bendtsen, J.** (2019) Vertical distribution of phytoplankton and primary production in relation to nutricline depth in the open ocean. *Mar. Ecol. Prog. Ser.*, **620**, 33–46.

Rilov, G. (2013) Regional extinctions and invaders' domination: an ecosystem phase-shift of Levant reef. *Rapp. Comm. Int. Pour l'Exploration Sci. Mér Méditerranée*, **40**, 782–783.

Rilov, G. (2016) Multi-species collapses at the warm edge of a warming sea. *Sci. Rep.*, **6**, 36897.

Rilov, G. and **Galil, B.** (2009) Marine bioinvasions in the Mediterranean Sea – history, distribution and ecology. In: *Biological Invasions in Marine Ecosystems Ecological Studies (Analysis and Synthesis)* (Eds Rilov, G. and Crooks, J.A.), Vol. **204**, pp. 549–575. Springer, Berlin, Heidelberg.

Rilov, G., **Peleg, O.**, **Yeruham, E.**, **Garval, T.**, **Vichik, A.** and **Raveh, O.** (2018) Alien turf: overfishing, overgrazing and invader domination in south-eastern Levant reef ecosystems. *Aquat. Conserv. Mar. Freshwat. Ecosyst.*, **28**, 351–369.

Rocha, L.A., **Pinheiro, H.T.**, **Shepherd, B.**, **Papastamatiou, Y.P.**, **Luiz, O.J.**, **Pyle, R.L.** and **Bongaerts, P.** (2018) Mesophotic coral ecosystems are threatened and ecologically distinct from shallow water reefs. *Science*, **361**, 281–284.

Sade, A., **Hall, J.K.**, **Golan, A.**, **Amit, G.**, **Gur-Arie, L.**, **Tibor, G.**, **Ben-Avraham, Z.**, **Hübscher, C.** and **Ben-Dor, E.** (2006) *High Resolution Bathymetry of the Mediterranean Sea off Northern Israel*. GSI report GSI/20/2006, IOLR report H44/2006, p. 1. Geological Survey of Israel, Jerusalem, Israel.

Sala, E., **Kizilkaya, Z.**, **Yildirim, D.** and **Ballesteros, E.** (2011) Alien marine fishes deplete algal biomass in the eastern Mediterranean. *PLoS One*, **6**, e17356.

Schmidt, C., **Titelboim, D.**, **Brandt, J.**, **Herut, B.**, **Abramovich, S.**, **Almogi-Labin, A.** and **Kucera, M.** (2016) Extremely heat tolerant photo-symbiosis in a shallow marine benthic foraminifera. *Sci. Rep.*, **6**, 30930.

Sherman, C., **Schmidt, W.**, **Appeldoorn, R.**, **Hutchinson, Y.**, **Ruiz, H.**, **Nemeth, M.**, **Bejarano, I.**, **Motta, J.J.C.** and **Xu, H.** (2016) Sediment dynamics and their potential influence on insular-slope mesophotic coral ecosystems. *Cont. Shelf Res.*, **129**, 1–9.

Shtienberg, G., **Dix, J.K.**, **Roskin, J.**, **Waldmann, N.**, **Bookman, R.**, **Bialik, O.M.**, **Porat, N.**, **Taha, N.** and **Sivan, D.** (2017) New perspectives on coastal landscape reconstruction during the Late Quaternary: a test case from central Israel. *Palaeogeogr. Palaeoclimatol. Palaeoecol.*, **468**, 503–519.

Silva, M. and **MacDonald, I.** (2017) Habitat suitability modeling for mesophotic coral in the northeastern Gulf of Mexico. *Mar. Ecol. Prog. Ser.*, **583**, 121–136.

Sisma-Ventura, G., **Yam, R.** and **Shemesh, A.** (2014) Recent unprecedented warming and oligothrophy of the Eastern Mediterranean Sea within the last millennium. *Geophys. Res. Lett.*, **41**, 5158–5166.

Sisma-Ventura, G., **Yam, R.**, **Kress, N.** and **Shemesh, A.** (2016) Water column distribution of stable isotopes and carbonate properties in the {South}-eastern {Levantine} basin ({Eastern} {Mediterranean}): {Vertical} and temporal change. *J. Mar. Syst.*, **158**, 13–25.

Solodoch, A., **Barkan, R.**, **Verma, V.**, **Gildor, H.**, **Toledo, Y.**, **Khain, P.** and **Levi, Y.** (2023) Basin-scale to submesoscale variability of the east Mediterranean sea upper circulation. *J. Phys. Oceanogr.*, **53**, 2137–2158.

Sørensen, O.J.R., **van Rijn, I.**, **Einbinder, S.**, **Nativ, H.**, **Scheinin, A.**, **Zemah-Shamir, Z.**, **Bigal, E.**, **Livne, L.**, **Tsemel, A.**, **Bialik, O.M.**, **Papeer, G.**, **Tchernov, D.** and **Makovsky, Y.** (2025) Bridging the gap in deep seafloor management: ultra fine-scale ecological habitat characterization of large seascapes. *Remote Sens. Ecol. Conserv.*, **11**, 472–489.

Stambler, N. (2014) The Mediterranean sea – primary productivity. In: *The Mediterranean Sea* (Eds Goffredo, S. and Dubinsky, Z.), pp. 113–121. Springer Netherlands, Dordrecht.

Storlazzi, C., **Storlazzi, C.D.**, **Ogston, A.S.**, **Bothner, M.H.**, **Field, M.E.**, **Presto, M.K.**, **Ogston, A.**, **Bothner, M.**, **Field, M.** and **Presto, M.** (2004) Wave- and tidally-driven flow and sediment flux across a fringing coral reef: southern Molokai, Hawaii. *Cont. Shelf Res.*, **24**, 1397–1419.

Stow, D.A.V., **Hernández-Molina, F.J.**, **Llave, E.**, **Sayago-Gil, M.**, **Díaz del Río, V.** and **Branson, A.** (2009) Bedform-velocity matrix: the estimation of bottom current velocity from bedform observations. *Geology*, **37**, 327–330.

Studivan, M.S. and **Voss, J.D.** (2018) Population connectivity among shallow and mesophotic Montastraea cavernosa corals in the Gulf of Mexico identifies potential for refugia. *Coral Reefs*, **37**, 1183–1196.

Talley, L.D., **Pickard, G.L.**, **Emery, W.J.** and **Swift, J.H.** (2011) *Descriptive Physical Oceanography: an Introduction*, 6th edn, p. 983. Elsevier – Academic Press, Amsterdam.

Thingstad, T.F., **Krom, M.D.**, **Mantoura, R.F.C.**, **Flaten, G.A.F.**, **Groom, S.**, **Herut, B.**, **Kress, N.**, **Law, C.S.**, **Pasternak, A.**, **Pitta, P.**, **Psarra, S.**, **Rassoulzadegan, F.**, **Tanaka, T.**, **Tselepides, A.**, **Wassmann, P.**, **Woodward, E.M.S.**, **Riser, C.W.**, **Zodiatis, G.** and **Zohary, T.** (2005) Nature of phosphorus limitation in the ultraoligotrophic eastern Mediterranean. *Science*, **309**, 1068–1071.

Tsemel, A., **Martinez, S.**, **Einbinder, S.**, **Nativ, H.**, **Deveto, A.**, **Sørensen, O.**, **Izhaki, I.** and **Tchernov, D.** (2025) Deep refuges: the distribution of marine fish in warming subtropics. Authorea. https://doi.org/10.22541/au.174188362.23468421/v1.

Valle-Levinson, A., **Kourafalou, V.H.**, **Smith, R.H.** and **Androulidakis, Y.** (2020) Flow structures over mesophotic coral ecosystems in the eastern Gulf of Mexico. *Cont. Shelf Res.*, **207**, 104219.

van Haren, H. (2017) Internal waves and bedforms. In: *Atlas of Bedforms in the Western Mediterranean* (Eds Guillén, J., Acosta, J., Chiocci, F. and Palanques, A.), pp. 25–28. Springer International Publishing, Cham.

Varzi, A.G., **Fallati, L.**, **Savini, A.**, **Bracchi, V.A.**, **Bazzicalupo, P.**, **Rosso, A.**, **Sanfilippo, R.**, **Bertolino, M.**, **Muzzupappa, M.** and **Basso, D.** (2023) Geomorphology of coralligenous reefs offshore southeastern Sicily (Ionian Sea). *J. Maps*, **19**, 1–13.

Vasilief, I. (2010) QtiPlot – data analysis and scientific visualisation.

Wall, M., **Schmidt, G.M.**, **Janjang, P.**, **Khokiattiwong, S.** and **Richter, C.** (2012) Differential impact of monsoon and large amplitude internal waves on coral reef development in the Andaman Sea. *PLoS One*, **7**, e50207.

Wang, Y.-H., **Dai, C.-F.** and **Chen, Y.-Y.** (2007) Physical and ecological processes of internal waves on an isolated reef ecosystem in the South China Sea. *Geophys. Res. Lett.*, **34**, L18609.

Wentworth, C.K. (1922) A scale of grade and class terms for clastic sediments. *J. Geol.*, **30**, 377–392.

Wickham, H. (2009) *ggplot2*, p. 213. Springer New York, New York, NY.

Wilckens, H., **Schwenk, T.**, **Lüdmann, T.**, **Betzler, C.**, **Zhang, W.**, **Chen, J.**, **Hernández-Molina, F.J.**, **Lefebvre, A.**, **Cattaneo, A.**, **Spieß, V.** and **Miramontes, E.** (2023) Factors controlling the morphology and internal sediment architecture of moats and their associated contourite drifts. *Sedimentology*, **70**, 1472–1495.

Williams, D.M., **Wolanski, E.** and **Andrews, J.C.** (1984) Transport mechanisms and the potential movement of planktonic larvae in the central region of the Great Barrier Reef. *Coral Reefs*, **3**, 229–236.

Wolanski, E. and **Delesalle, B.** (1995) Upwelling by internal waves, Tahiti, French Polynesia. *Cont. Shelf Res.*, **15**, 357–368.

Woodson, C.B. (2018) The fate and impact of internal waves in nearshore ecosystems. *Annu. Rev. Mar. Sci.*, **10**(1), 421–441.

Wyatt, A.S.J., **Leichter, J.J.**, **Toth, L.T.**, **Miyajima, T.**, **Aronson, R.B.** and **Nagata, T.** (2020) Heat accumulation

on coral reefs mitigated by internal waves. *Nat. Geosci.*, **13**, 28–34.

Wynn, R.B. and **Stow, D.A.V.** (2002) Classification and characterisation of deep-water sediment waves. *Mar. Geol.*, **192**, 7–22.

Yahel, R., **Yahel, G.** and **Genin, A.** (2002) Daily cycles of suspended sand at coral reefs: a biological control. *Limnol. Oceanogr.*, **47**, 1071–1083.

Manuscript received 2 February 2025; revision accepted 1 December 2025

Supporting Information

Additional information may be found in the online version of this article:

Figure S1.1 A comparison of Synthetic Aperture Sonar imagining of port and starboard side of the AUV, Arrows indicate direction of illumination by the sonar.

Figure S1.2. The effects of transit direction (white arrow) on visualisation of seafloor features.

Figure S1.3. Additional imaging of reef surface and biological coverage.

Figure S1.4. General 3D shaded relief views of the Bustan Hagalil Ridge, visualised from the south-west (a), north-east (b) and south-east (c). The black arrow of the three axes (center) points to the north.

Figure S1.5. An example of the multibeam bathymetry (a), and the same with an overlay of the SAS backscatter. Note that the bedform on the righthand side are only visible with the SAS imagery.

Figure S1.6. Example of individual biological elements visible with SAS imagery. Small white arrows indicate individual elements (possible branching bryozoans, coralline algae, sponges or corals) raising over the horizon of individual solitary reefs, visible over the shadow of the reef.

Figure S1.7. A composite image of the study area with shaded relief bathymetry of the Bustan Hagalil reef overlaid with (white dashed polygon) Alos2 SAR L band, HH polarity, acquired on 5 January 2019 in DN (digital numbers) proportional to $\gamma 0$ backscatter (source https://www.eorc.jaxa.jp/). The co-polarised SAR data reveals wavy features, which are suggested to be the surface manifestation of internal waves. A profile going through the SAR imagery (red line) reveals that these wavy features have wavelengths of ~100–500 m.

Appendix S2. Coordinates (ITM) and shape parameters for badforms.

Appendix S3. Estimation of effective wave depth.

Appendix S4. Brunt-Väisälä frequency distribution in the study region.

Appendix S5. Wave parameters in the study region.